

Generating large volumes of crust-derived high $\delta^{18}\text{O}$ rhyolites in the Chon Aike Silicic Large Igneous Province, Patagonia

Michelle L. Foley¹, Benita Putlitz¹, Lukas P. Baumgartner¹, Florence Bégué², Guillaume Siron^{3,4}, and Andres Kosmal⁵

¹Institute of Earth Sciences, University of Lausanne, UNIL-Mouline, 1015 Lausanne, Switzerland

²Department of Earth Sciences, University of Geneva, Rue des Maraichers 13, 1205 Geneva, Switzerland

³WiscSIMS, Department of Geosciences, University of Wisconsin-Madison, Madison, Wisconsin 53706, USA

⁴Department of Biological, Geological, and Environmental Sciences, University of Bologna, 40126 Bologna, Italy

⁵Costanera Norte 46, El Chaltén 9301 Santa Cruz, Argentina

GEOSPHERE, v. 19, no. 4

<https://doi.org/10.1130/GES02551.1>

15 figures; 3 tables; 1 set of supplemental files

CORRESPONDENCE: michellefoley118@gmail.com

CITATION: Foley, M.L., Putlitz, B., Baumgartner, L.P., Bégué, F., Siron, G., and Kosmal, A., 2023, Generating large volumes of crust-derived high $\delta^{18}\text{O}$ rhyolites in the Chon Aike Silicic Large Igneous Province, Patagonia: *Geosphere*, v. 19, no. 4, p. 975–1005, <https://doi.org/10.1130/GES02551.1>.

Science Editor: Shanaka de Silva
Guest Associate Editor: Jonathan S. Miller

Received 20 May 2022
Revision received 8 March 2023
Accepted 21 March 2023

Published online 19 May 2023



This paper is published under the terms of the CC-BY-NC license.

© 2023 The Authors

ABSTRACT

The Jurassic Chon Aike Silicic Large Igneous Province (Patagonia and the Antarctic Peninsula) is dominated by voluminous, crust-derived magmas (235,000 km³) that erupted as predominately explosive silicic material over ~40 m.y. In this study, we combine petrological descriptions and bulk-rock major- and trace-element compositions with quartz oxygen-isotope measurements from multiple silicic units (primarily ignimbrites and some rhyolitic flows) from two of the five silicic formations in Patagonia. We have identified that quartz oxygen-isotope values are high (>9‰–12‰). Quartz phenocrysts analyzed by secondary ion mass spectroscopy (SIMS) are also homogeneous at the microscale with no measurable change in isotope value with respect to internal and often complex zoning textures. The ubiquity of widespread high $\delta^{18}\text{O}$ rhyolites and their trace-element compositions support their origin from melting of a metasedimentary source with a similarly high $\delta^{18}\text{O}$ value. Mass balance calculations require that an average of >75% melt derived from partial melting of the dominant basement lithology is needed to explain the isotopic and chemical composition of the rhyolites. The ideal *P-T* environment was identified by thermodynamic models for fluid-absent melting of graywackes at 900 °C and 5 kbar. Regional-scale crustal melting occurred during a widespread, high heat-flux environment within an extensional setting during the break-up of the Gondwanan supercontinent. The overlap of a unique tectonic and igneous environment, combined with a fertile crust dominated by graywacke and pelitic compositions in southern Patagonia, generated large volumes of some of the highest $\delta^{18}\text{O}$ silicic magmas documented in the geologic record.

INTRODUCTION

Observations in various intraplate and arc volcanic settings show that silicic (>70 wt% bulk SiO₂) magmatic systems evolve via a spectrum between the two end members: (1) fractional crystallization of a mantle-derived melt or

(2) by partial melting of the crust (Lipman et al., 1978; DePaolo, 1981; Hildreth et al., 1991; DePaolo et al., 1992; Clemens et al., 2020; Moyen, 2020; Jacob et al., 2021; Moyen et al., 2021). The Chon Aike Silicic Large Igneous Province (CASP) is one of the few examples in which ~235,000 km³ of predominately explosive silicic magmas are suggested to be derived by widespread crustal melting during a series of magmatic flareup events over a protracted period of ~40 m.y. (Kay et al., 1989; Pankhurst and Rapela, 1995; Pankhurst et al., 1998; Féraud et al., 1999; Pankhurst et al., 2000; Riley et al., 2001; Bastias et al., 2021). A significant crustal component has been supported by evidence from radiogenic Nd and Sr bulk-isotope values (Pankhurst and Rapela, 1995; Parada et al., 1997; Bouhier et al., 2017; Zaffarana et al., 2020; Strazzere et al., 2022) and by some oxygen-isotope data of bulk rock, quartz, and zircon (Riley et al., 2001; Seitz et al., 2018a). However, isotope data are limited considering the size of the province, and additional data are required to trace the crustal sources involved in the magma generation and their proportions.

In this study, we focus on the $\delta^{18}\text{O}$ values of ubiquitous quartz phenocrysts since the mineral preserves its original magmatic oxygen-isotope value, despite widespread secondary alteration in the province (e.g., Riley et al., 2001; Seitz et al., 2018a). Secondly, we compare the new $\delta^{18}\text{O}$ magmatic values with the isotope values of the basement lithology to reevaluate the origin and evolution of the CASP. Since the Earth's surface exhibits a large range of $\delta^{18}\text{O}$ values (e.g., –65 to +30; Sharp, 2006), involvement of crustal melting reservoirs can have a distinct oxygen-isotope composition in comparison to the mantle, which has a homogeneous $\delta^{18}\text{O}$ of 5.5 ± 0.2‰ (Matthey et al., 1994; Eiler, 2001). For example, near-surface weathering generates materials (e.g., sediments) with distinctly high $\delta^{18}\text{O}$, up to ~30‰ (Savin and Epstein, 1970). These $\delta^{18}\text{O}$ values are not significantly changed during metamorphism or melting, due to the high abundance of oxygen in silicate rocks (~50 wt%) and the low fractionation of oxygen isotopes at elevated temperatures (e.g., >700 °C). Hence, their metamorphosed counterparts (i.e., metapelites and metagraywackes) contribute their bulk oxygen-isotope compositions to melting regions and can be traced using the oxygen-isotope compositions of the erupted materials.

The $\delta^{18}\text{O}$ values of erupted rhyolites have been widely used to distinguish between the two end-member processes that lead to the production of large

Michelle Foley <https://orcid.org/0000-0003-4420-2416>

volumes of silicic magmas. In some cases, bulk crustal melting is invoked leading to the generation of high $\delta^{18}\text{O}$ granites with values up to 11.5‰–13.0‰ in the Himalayan Granitoids (Blattner et al., 1983), the “S-type granites” in the Lachlan Fold Belt of Australia (Chappell and White, 1992), and the Cape Granites in South Africa (Harris et al., 1997). However, a pure crustal source is less commonly invoked for generating eruptible, silica-rich magmas, largely due to the thermal constraints of crustal anatexis and/or processes of assimilation (e.g., Glazner, 2007; Heinonen et al., 2022). Many high $\delta^{18}\text{O}$ rhyolites are interpreted to be generated via mantle melting with significant crustal assimilation from 10% to 50% by volume (e.g., 7‰–9‰ $\delta^{18}\text{O}$: Okataina Volcanic Center [New Zealand], Sas et al., 2022; Altiplano-Puna Volcanic Complex and Cerro Galan [Chile], Folkes et al., 2013; González-Maurel et al., 2020; Toba Tuff [Indonesia], Bindeman and Simakin, 2014; Budd et al., 2017; Bishop Tuff [California, USA] and Fish Canyon Tuff [Colorado, USA], Bindeman and Valley, 2002).

High $\delta^{18}\text{O}$ magmas (>6.4‰) themselves do not appear to be rare, suggesting crustal melting and assimilation are indeed important in the generation of many silicic magmas. However, particularly large volumes of high $\delta^{18}\text{O}$ rhyolites are uncommon in the geologic record. In this study, we show that a large part of the CASP is predominantly crustal in origin by combining petrological descriptions and bulk-rock major- and trace-element compositions with quartz and bulk-rock oxygen-isotope data. We focus on two of the five silicic formations of the CASP in Patagonia, which include the El Quemado Complex (EQC) and the Chon Aike Formation (CA) (Fig. 1A). To constrain the potential melting sources for these rhyolites and provide a framework for the necessary conditions (e.g., source rock type and $P\text{-}T\text{-}H_2\text{O}$) that can generate such large volumes of eruptible silicic magma, we also present petrologic descriptions, major- and trace-element geochemistry, and the first bulk-rock oxygen-isotope measurements of the local basement lithology.

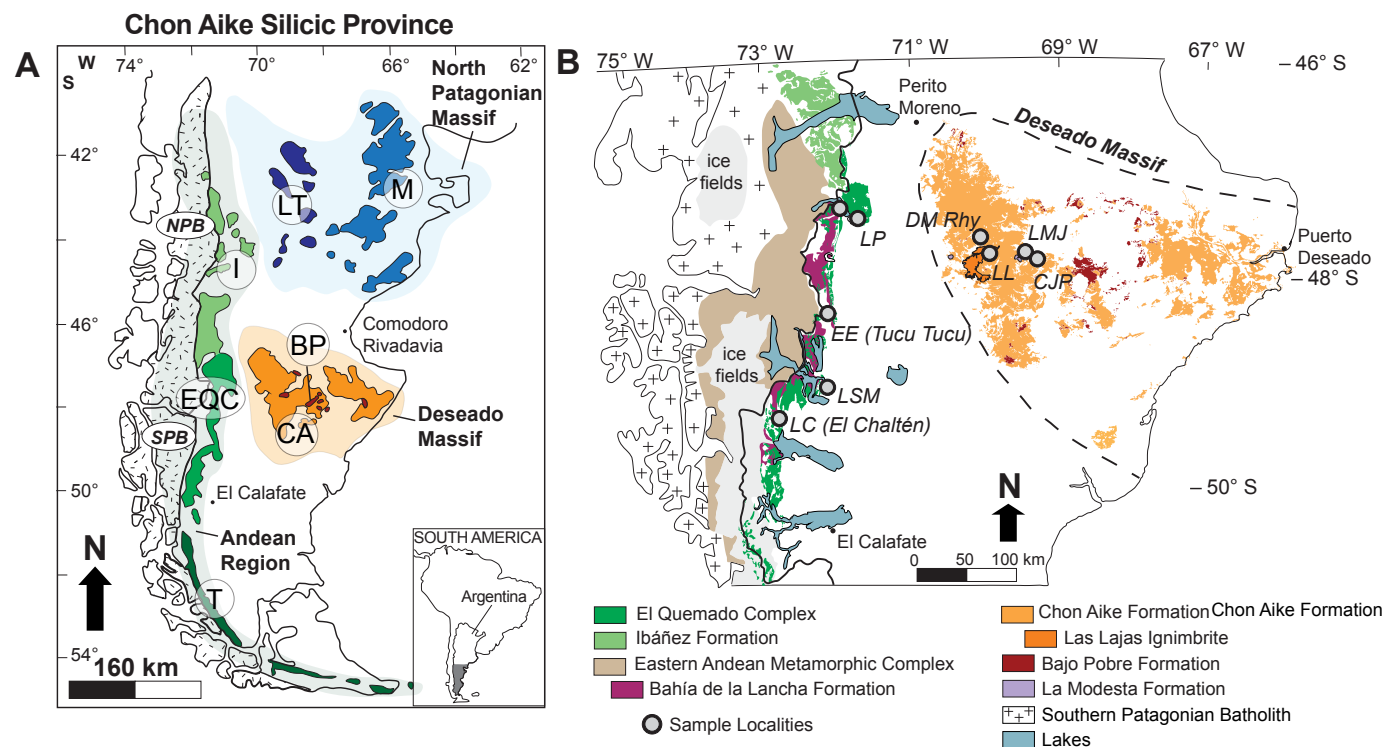


Figure 1. (A) Simplified overview of the seven formations of the Chon Aike Silicic Province in Patagonia, including both the silicic and minor andesitic and/or trachyandesitic units—Lonco Trapial (LT) and Bajo Pobre Formations (BP), and the Southern Patagonian Batholith (SPB) and Northern Patagonian Batholith (NPB). Abbreviations: M—Marifil Formation; I—Ibáñez Formation; CA—Chon Aike Formation; EQC—El Quemado Complex; T—Tobifera Formation. (B) Detailed geologic map with sample localities, based on the maps provided by the Argentine Geological Mining Service and National Geology and Mining Service of Chile. Abbreviations for sample localities: LP—Lago Posadas; EE—Estancia Ensenada; LSM—Lago San Martín; LC—Los Cóndores; DM Rhy—Deseado Massif Rhyolite; LL—Las Lajas; LMJ—La Josefina Dome; and CJP—Cerro Jorge Paz.

■ GEOLOGIC BACKGROUND

Chon Aike Silicic Large Igneous Province

The CASP groups together several major formations spread throughout Patagonia and the Antarctic Peninsula (Fig. 1A). The province covers an area of ~700,000 km² with an estimated volume of ~235,000 km³ (Pankhurst and Rapela, 1995; Pankhurst et al., 1998). The volcanic rocks are dominated by rhyolite compositions that are primarily erupted as ignimbrites (~80% of total deposits) of variable thickness, but some interspersed rhyolitic lava flows and domes were recognized (e.g., Seitz et al., 2018a; Navarrete et al., 2020; Navarrete, 2021; Foley et al., 2022a). The remaining compositions range from andesitic to dacite, but a general bimodal association between rhyolite and andesite compositions exists for the province.

The volcanic rocks of the Marifil and Chon Aike Formations tend to be single, flat-lying undeformed ignimbrites of variable thickness (up to ~100 m thick; Pankhurst et al., 1998). These ignimbrites follow the topography, whereas the EQC typically comprises a stack of several conformable ignimbrites (Fig. 2). Correlations between distant ignimbrite outcrops throughout southern Patagonia are challenging due to poor exposures and facies variations, but recent detailed mapping has further subdivided the many volcanic rocks of the CASP, revealing that often numerous and typically small-volume eruptions predominate (<100 km³) (e.g., Moreira et al., 2009; Sruoga et al., 2014; Echeveste et al., 2020; Navarrete et al., 2020; Matthews et al., 2021).

Volcanism in the CASP occurred over a time interval of 40 m.y. in response to a period of extension during the initial breakup of Gondwana (ca. 146–190 Ma; Pankhurst et al., 2000; Poblete et al., 2014; Pavón Pivetta et al., 2020; Strazzere et al., 2022). The major units of the CASP can be subdivided into major peaks of volcanic activity (Pankhurst et al., 2000): V1 (188–178 Ma), V2 (172–167 Ma), and V3 (162–153 Ma). Volcanism in the North Patagonian Massif started in the northeast with the eruption of the silicic Marifil Formation (V1) and continued to the west with the eruptions of the predominately andesitic lavas of the Lonco Trapial Formation (ca. 178 Ma) (Fig. 1A); in the Antarctic Peninsula, the eruptions of the Mount Poster and Brennecke Formations are coeval during the V1 episode. Volcanism proceeded southward into the Deseado Massif with the eruptions of the (V2) silicic Chon Aike Formation and andesitic Bajo Probe Formation of Patagonia and the silicic Mapple Formation of the Antarctic Peninsula. The youngest erupted units (V3) are restricted to the eastern front of the Andean Cordillera and include the EQC and its equivalent formations in Chile, locally the Ibañez (Baker et al., 1981) and Tobífera (Fig. 1A). Recent U-Pb zircon crystallization ages of the EQC and Ibañez Formation extend the Late Jurassic CASP magmatism until ca. 146 Ma (e.g., Poblete et al., 2014; Foley et al., 2022a).

Despite their compositional and temporal difference, the partial overlap in time between the Marifil Formation (V1) with the voluminous basalts of the Karoo and Ferrar Large Igneous Provinces in Southern Africa and Antarctica was used to argue a genetic relationship of volcanism in Patagonia with the

thermal anomaly associated with the Discovery-Shona-Bouvet group of mantle plumes (Storey and Kyle, 1997; Pankhurst et al., 2000; Riley et al., 2001; Storey et al., 2013; Navarrete et al., 2019). While there is no strong evidence for large volumes of mantle-derived magma in southern Patagonia itself, the plume is hypothesized to provide a source of external heat to drive intraplate magmatism by the above authors. The V2 and V3 volcanic rocks would represent a westward migration away from the proposed mantle plume head, toward the paleo-Pacific margin of Gondwana (Pankhurst et al., 2000; Riley and Knight, 2001). The youngest volcanic rocks of the V3 overlap with the range of the initial plutons in the Southern Patagonian Batholith, which is related to normal subduction of the Pacific Ocean floor beneath the South American continent (ca. 150 Ma; Hervé et al., 2007).

The predominance of silicic units over minor contemporary andesites, in combination with major- and trace-element changes (higher Ba, Sr, and Ba/Rb and lower Rb, Zr, and Rb/Sr with increasing SiO₂) and the peraluminous composition, was used to suggest crustal anatexis as the primary source of magma for the province (Baker et al., 1981; Gust et al., 1985). Radiogenic studies further invoke a petrogenetic model of lower-crustal anatexis for the CASP, where widespread initial ⁸⁷Sr/⁸⁶Sr values (0.7067 ± 0.0003) combined with initial εNd of ~-4 (±2) were measured throughout Patagonia (Pankhurst and Rapela, 1995; Riley et al., 2001). Initial εNd values of -7.1 to -8.7 measured in the Jurassic rhyolites of the Antarctic Peninsula indicate a common petrogenesis with the V1 CASP formations of Patagonia (Wever and Storey, 1992; Riley et al., 2001). Though less radiogenic, values of initial εNd (-2 to -3) measured in the Mapple Formation and Chon Aike Formation (V2) likely reflect heterogeneities in crustal source contributions within Patagonia and the Antarctic Peninsula (Riley et al., 2001).

Existing stable isotope studies within the CASP are relatively rare (e.g., Riley et al., 2001; Seitz et al., 2018a). The earliest oxygen-isotope study indicated a wide range of quartz δ¹⁸O values (6.4‰–10.6‰) for eight samples of the Mapple Formation of the Antarctic Peninsula (Riley et al., 2001). The units with the highest quartz δ¹⁸O (10.2‰–10.6‰) have supporting crust-like radiogenic isotope compositions, with the highest initial ⁸⁷Sr/⁸⁶Sr (0.7070–0.7076) and most negative initial εNd (-3.2 to -3.6) measured in the formation (Riley et al., 2001). Oxygen-isotope data for the area surrounding the town of El Chaltén in southern Patagonia yielded high δ¹⁸O values for quartz (10.9‰–12.5‰) and zircon (7.5‰–10.1‰) measured in multiple volcanic rocks of the EQC, indicating a significant crustal contribution in the source of the melts in all samples (Seitz et al., 2018a).

Paleozoic Basement

Within the southern Andes, the oldest exposed units are the Carboniferous–Devonian Gondwanan basement of the Eastern Andean Metamorphic Complex (EAMC), composed of low-grade, quartz-rich turbidite units (Hervé et al., 2003; Augustsson et al., 2006; Hervé et al., 2008; Giacosa et al., 2012) (Fig. 1B). The

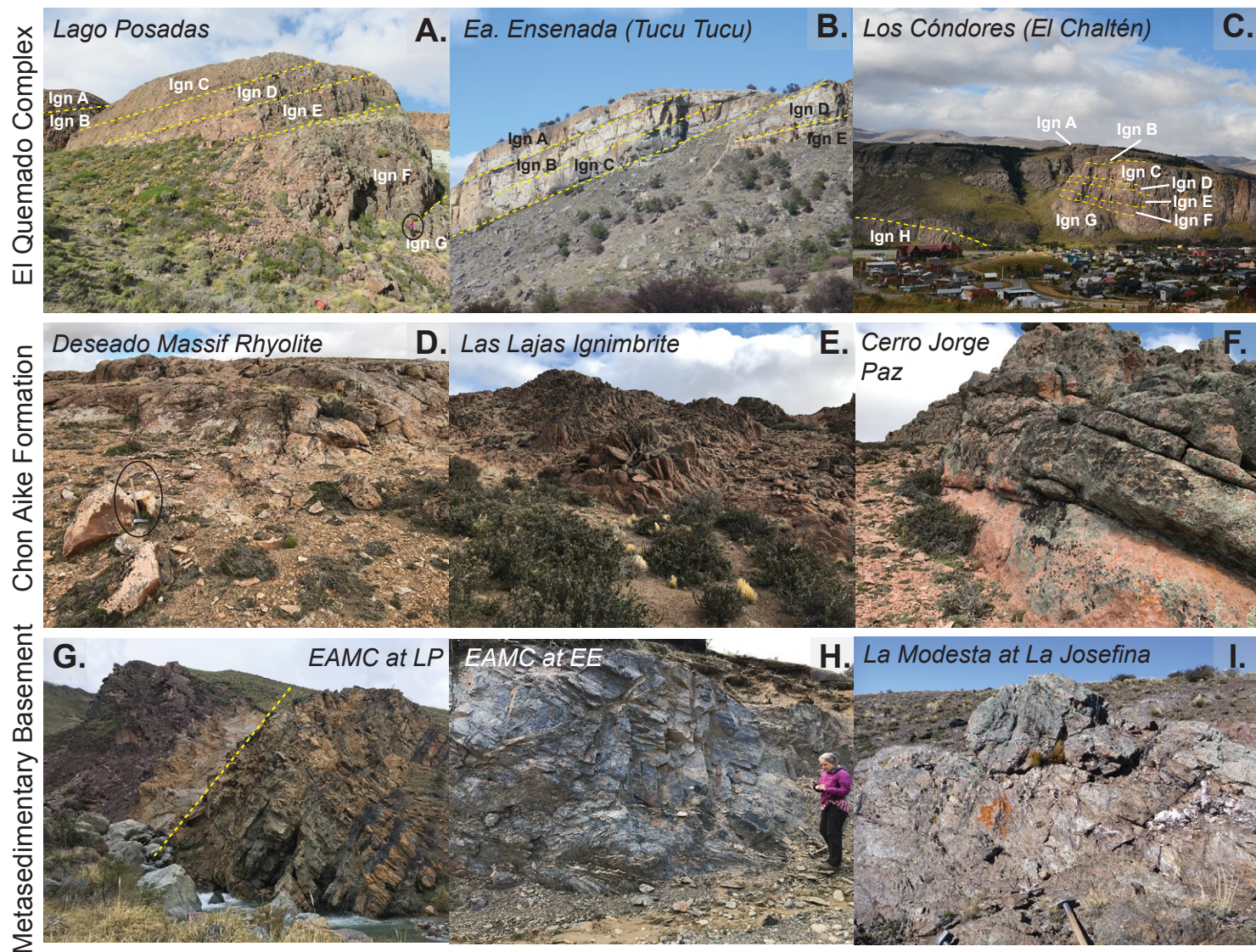


Figure 2. Studied field locations. A comparison between the El Quemado Complex (EQC) and Chon Aike Formation (CA) volcanic units shows that (A–C) the EQC comprises several ignimbrite (ign) sequences that are typically tilted due to the Andean orogeny, whereas (D–F) the CA comprises single, flat-lying volcanic units that follow topography. (G) Turbidite sequences of alternating graywacke and shales from the Eastern Andean Metamorphic Complex (EAMC) at Lago Posadas (LP) are unconformably overlain by the Jurassic EQC (alteration prevalent by the deep-red coloration), (H) Greenschist-facies pelites of the Bahía de la Lancha at Ea. Ensenada (EE; B. Putlitz for scale). (I) Greenschist facies graywackes of the La Modesta Formation at the La Josefina locality; sledgehammer for scale.

EAMC has been assigned multiple names throughout the regions of Argentina and Chile, but the dominant formation includes the Bahía de la Lancha Formation. In much of the eastern sector of the southern Patagonian Andes, the Bahía de la Lancha is unconformably overlain by late Jurassic volcanic units of the EQC (Fig. 2G).

Outcrops of basement rock in the extra-Andean region of southern Patagonia are confined to relatively small areas within the Deseado Massif (Fig. 1B). They are sparsely exposed due to basin formation during Triassic extension, the intrusion of Late Triassic calc-alkaline inner cordilleran batholiths, the extensive rhyolite volcanism of the CASP during the Jurassic rifting of Gondwana, and shallow marine basin sedimentation during the Cretaceous (Pankhurst et al., 2003) (Fig. 1B). In the western Deseado Massif, the basement exposures include the low-grade, Late Paleozoic metasedimentary units of the La Modesta and Cerro Negro Formations. The La Modesta Formation contains alternating pelitic and psammitic muscovite-chlorite schists and meta-quartzites, with minor calc-silicate rocks, basic metavolcanics, and exhalative rocks (graphitic tourmalinites, tourmaline-bearing schists, and Fe-Mn-enriched horizons) (Moreira et al., 2013). The main protolith is interpreted to be a pelitic and psammitic pelitic marine sedimentary sequence (Moreira et al., 2013). The Cerro Negro Formation is similar to the La Modesta Formation in composition, dominated by quartz-muscovite-chlorite schists. Only a younger maximum depositional age (ca. 380 versus 446 Ma) distinguishes the two formations from each other in the western Deseado Massif (Permuy-Vidal et al., 2014).

METHODS

Sample Selection and Petrography

A total of 41 samples were collected from 28 eruptive units in the CASP (Table 1 and Fig. 1B). Our sampling strategy provides an opportunity to evaluate the potential changes in CASP magmatic evolution across both time and space on two levels: (1) the overall change between the younger (ca. 150 Ma) EQC of the eastern Andean margin with the slightly older (ca. 160 Ma) CA formation in the western Deseado Massif and (2) comparing the changes through time within multiple ignimbrite sequences, sampled from north to south along an ~230 km transect of the EQC (Figs. 1B and 2). Volcanic rocks were sampled from predominately ignimbrites ($n = 26$) and two rhyolite lavas ($n = 2$). In addition, basement metasediments to the EQC and the CA were sampled from three localities throughout southern Patagonia.

Petrographic descriptions of each sample were completed via both hand-sample and petrographic microscope examination. All samples were cut into two mirrored-halves, in which one half was processed for bulk-rock major- and trace-elements measurements by X-Ray fluorescence (XRF) and laser ablation-inductively coupled plasma-mass spectrometry (LA-ICP-MS), respectively, and the other half was coarsely crushed for selection of bulk quartz mineral

separates. In addition, 14 metasedimentary samples were cut and crushed into a powder using a tungsten mill for bulk-oxygen measurements by laser fluorination and for bulk-rock major-element analyses.

Major- and Trace-Element Geochemistry

Whole-rock major-element contents (SiO_2 , TiO_2 , Al_2O_3 , Fe_2O_3 , MnO , MgO , CaO , Na_2O , K_2O , Cr_2O_3 , and NiO) were determined by X-ray fluorescence (XRF) at the University of Lausanne, using a wavelength-dispersive PANalytical Axios^{mAX} spectrometer fitted with a 4 kW Rh X-ray tube. The analyses were performed on fused disks prepared from 1.2 g of calcined sample powder mixed with lithium-tetraborate (1:5 mixture). The XRF calibrations are based on 21 international silicate rock reference materials. The loss on ignition (LOI) was measured after calcination of the sample powders for 2 h at 1050 °C. Trace-element analyses (Sc, V, Cr, Mn, Co, Ni, Cu, Zn, Ga, Ge, As, Se, Br, Rb, Sr, Y, Zr, Nb, Mo, Ag, Cd, Sn, Sb, Te, I, Cs, Ba, La, Ce, Nd, Sm, Yb, Hf, Ta, W, Hg, Tl, Pb, Bi, Th, and U) were conducted on disks obtained by pressing 12 g of sample powder on a support of 3 g of Hoechst-wax-C. The trace-element calibrations are based on synthetic geological reference materials and international silicate rock reference materials. The limits of detection depend on the element concerned but are in the range 1–7 ppm for trace elements and 20–80 ppm for major elements.

The XRF analyses were complemented by trace-element analyses (Sc, Co, Ni, Zn, Rb, Sr, Y, Zr, Nb, Mo, Cs, Ba, Hf, Ta, W, Pb, Th, U, and lanthanides) of the lithium tetraborate fused disks using LA-ICP MS. The LA-ICP-MS facility consists of an Agilent 7700x quadrupole spectrometer coupled with a GeoLas 200M 193 nm ArF excimer ablation system at University of Lausanne (UNIL). Ablation parameters included a repetition rate of 10 Hz, fluence of 6 J/cm², and spot size of 120 µm. Helium was used as the carrier gas. The National Institute of Standards and Technology standard reference material 612 soda-lime-silica glass was used as the primary standard. The BCR-2G glass was measured as the secondary standard. Each sample was ablated three times; the trace-element abundances were calculated offline using LAMTRACE (Jackson, 2008); ²⁷Al was used as the internal standard, using the Al_2O_3 wt% contents determined by XRF, prior to trace-element collection. The statistics associated with the repeatability of the three spots per sample are listed in File S1¹. Bulk-rock analyses are normalized to anhydrous compositions for discussion and graphical representations.

For quartz mineral separation, bulk ignimbrite and rhyolite samples were coarsely crushed to a size fraction of 500–1000 µm using a hydraulic press;

¹Supplemental Material. Includes data tables of bulk-rock geochemistry, oxygen isotope values by laser fluorination and secondary ion mass spectrometry, and thermodynamic model parameters. Figures of in situ oxygen isotope analyses overlain on quartz cathodoluminescence images. Figures of additional major and trace-element bulk geochemistry plots and SIMS oxygen isotope values plotted per sample. Please visit <https://doi.org/10.1130/GEOS.S.22484818> to access the supplemental material, and contact editing@geosociety.org with any questions.

TABLE 1. SUMMARY OF SAMPLE DESCRIPTIONS, INCLUDING LOCALITY, PHENOCRYST ASSEMBLAGE, AND MODAL ABUNDANCES

Sample	Formation	Member	Unit	Latitude (°S)	Longitude (°W)	Elevation (m)	Phenocryst assemblage	Phenocryst estimates (bulk tuff %)	
<u>Lago Posadas</u>									
LPMF1	El Quemado Complex	NA	Ign A	47.50114	71.76497	288	qtz, kfs, pl, bt, ox, zrn	7	
LPMF2		NA	Ign A	47.50114	71.76497	288	qtz, kfs, pl, bt, ox, zrn	7	
LPMF3		NA	Ign B	47.50114	71.76497	288	qtz, pl, kfs opx, ox, zrn	10	
LPMF4		NA	Ign C	47.50284	71.76550	255	qtz, kfs, bt, ox	7	
LPMF5		NA	Ign D	47.50282	71.76561	254	qtz, pl, kfs, bt, ox	5	
LPMF6		NA	Ign E	47.50281	71.76573	235	pl, qtz, ox	7	
LPMF7		NA	Ign F	47.50287	71.76581	237	qtz, pl, kfs, bt, ox	7	
LPMF8		NA	Ign F	47.50285	71.76588	232	qtz, pl, kfs, bt, ox	7	
LPMF9		NA	Ign F	47.50285	71.76588	232	qtz, pl, kfs, bt, ox,	5–7	
LPMF10		NA	Ign G	47.50300	71.76579	230	qtz, pl, kfs, bt, op, zrn	10	
LPMF11	Eastern Andean Metamorphic Complex	Bahía de la Lancha	Graywacke	47.37420	71.99140	477	pl, qtz, wm, bt, chl, ox	NA	
LPMF12		Bahía de la Lancha	Graywacke	47.37539	71.99120	499	pl, qtz, wm, bt, chl, ox	NA	
LPMF13		Bahía de la Lancha	Graywacke	47.37546	71.99148	509	pl, qtz, wm, bt, chl, ox	NA	
LPMF14		Bahía de la Lancha	Graywacke	47.37599	71.98684	463	pl, qtz, wm, bt, chl, ox	NA	
<u>Estancia (Ea.) Ensenada (Tucu Tucu)</u>									
EEMF10	El Quemado Complex	NA	Ign A	48.34457	72.17326	722	pl, qtz, op, zrn	15	
EEMF11		NA	Ign B	48.34446	72.17402	715	qtz, pl, kfs, zrn	5	
EEMF12		NA	Ign B	48.34440	72.17402	710	qtz, pl, ox	6	
EEMF7		NA	Ign C	48.34422	72.17713	716	qtz, kfs, pl, bt, ox, zrn	7	
EEMF8		NA	Ign D	48.34393	72.17610	697	pl, kfs, qtz, ox	15	
EEMF9		NA	Ign E	48.34912	72.17457	684	pl, kfs, qtz, bt, op, zrn	7	
EEMF6		NA	Ign F	48.34409	72.17766	679	qtz, kfs, bt, op, zrn	10	
EEMF4		NA	Ign G	48.34389	72.17778	664	qtz, kfs, bt, op, zrn	2	
EEMF1		Eastern Andean Metamorphic Complex	Bahía de la Lancha	Pelite	48.32059	72.19788	520	wm, chl, qtz, pl, ox	NA
EEMF2			Bahía de la Lancha	Pelite	48.32059	72.19788	520	wm, chl, qtz, pl, ox	NA
EEMF13	Bahía de la Lancha		Pelite	48.36882	72.06251	639	wm, chl, qtz, pl, ox	NA	
EEMF14	Bahía de la Lancha		Graywacke	48.36882	72.06251	639	pl, qtz, wm, bt, chl, ox	NA	
<u>Lago San Martín</u>									
LSMMF1	El Quemado Complex	NA	Ign	49.04843	72.22284	340	qtz, kfs, pl, bt, zrn	15	
<u>Los Cóndores (El Chaltén)</u>									
LCMF12	El Quemado Complex	NA	Ign A	49.32543	72.87860	628	qtz, pl, kfs, bt, op, zrn	5–7	
LCMF11		NA	Ign B	49.32499	72.87963	582	pl, qtz, bt, op, zrn	10–12	
LCMF8		NA	Ign C	49.32650	72.87978	568	qtz, pl, kfs, bt, op, ap, zrn	10	
LCMF7		NA	Ign C	49.32650	72.87978	568	qtz, pl, kfs, bt, zrn	10	
LCMF10		NA	Ign D	49.32538	72.87980	543	qtz, pl, kfs, bt, ox, ap, zrn	15	
LCMF6		NA	Ign E	49.32627	72.88031	526	pl, qtz, zrn	10	
LCMF4		NA	Ign F	49.32644	72.88067	479	qtz, pl, bt, ox, ap, zrn	12	
LCMF1		NA	Ign G	49.32748	72.88004	404	pl, qtz, bt, opx, ox, zrn	7	
LCMF14		NA	Ign H	49.32533	72.88345	405	qtz, pl, kfs, ox, zrn	7	

(continued)

TABLE 1. SUMMARY OF SAMPLE DESCRIPTIONS, INCLUDING LOCALITY, PHENOCRYST ASSEMBLAGE, AND MODAL ABUNDANCES (*continued*)

Sample	Formation	Member	Unit	Latitude (°S)	Longitude (°W)	Elevation (m)	Phenocryst assemblage	Phenocryst estimates (bulk tuff %)
<u>Deseado Massif (undifferentiated Chon Aike Formation)</u>								
DMMF1	Chon Aike	NA	Rhy	47.79647	70.18249	629	qtz, kfs, ox, zrn	5
DMMF2		NA	Rhy	47.79720	70.18178	636	qtz, kfs, ox, zrn	3
<u>Las Lajas Ignimbrite</u>								
LLMF1	Chon Aike	Las Lajas Ignimbrite	Vitrophyre	47.79966	69.90558	794	pl, kfs, qtz, bt, ox, zrn ± aln	15
LLMF2			Vitrophyre	47.79974	69.90607	806		20–25
LLMF3			Densely welded	47.79974	69.90607	806		17–20
LLMF4			Moderately welded	47.79918	69.91038	839		10
LLMF5			Moderately welded	47.79919	69.91254	849		15
LLMF6			Poorly welded	47.79915	69.90679	799		15
<u>La Josefina</u>								
LMJMF3	Chon Aike	La Josefina Dome	Rhy	47.84698	69.41317	767	qtz, kfs, pl, bt, zrn	<1
LMFMF9			Rhy	47.85684	69.41898	770		1–2
LMFMF10			Rhy	47.85684	69.41898	770		1–2
LMJMF1	La Modesta Formation	NA	Meta-volcanic	47.85535	69.42993	768	qtz, pl, chl, ep, tr, ox, cal	NA
LMJMF2		NA	Calc-silicate	47.85502	69.42902	769	qtz, pl, chl, ep, ox, cal	NA
LMJMF5		NA	Muscovite-chlorite schist	47.84808	69.42621	748	wm, chl, qtz, pl, cal	NA
LMJMF6a		NA	Meta-volcanic	47.84270	69.42623	746	qtz, pl, chl, ep, tr, ox, cal	NA
LMJMF7		NA	Meta-volcanic	47.84270	69.42623	746	qtz, pl, chl, ep, tr, ox, cal	NA
LMJMF8		NA	Meta-volcanic	47.84270	69.42623	746	qtz, pl, chl, ep, tr, ox, cal	NA
<u>Cerro Jorge Paz Ignimbrite</u>								
DMMF3	Chon Aike	Cerro Jorge Paz Member	Ign	47.89061	69.30384	719	qtz, kfs, bt, ox, zrn,	5

Notes: aln—allanite; ap—apatite; bt—biotite; cal—calcite; chl—chlorite; ep—epidote; kfs—K-feldspar; NA—not applicable; opx—orthopyroxene; ox—oxide; pl—plagioclase; qtz—quartz; tr—tremolite; wm—white mica; zrn—zircon; Rhy—rhyolite; Ign—ignimbrite.

this size fraction maximizes the point at which individual bulk quartz phenocrysts were picked and separated for laser fluorination (LF) analysis and for selection of secondary ion mass spectrometry (SIMS) analysis. Quartz was separated from the bulk tuff, as opposed to pumice clasts, largely due to the small volumes of individual pumice within samples; however, textural differences between the matrix and pumice quartz imaged within thin section were not observed. Bulk phenocrysts of quartz were mounted in epoxy and polished down to obtain a surface closest to the center of the quartz phenocrysts. To minimize topography-induced mass fractionation during the SIMS analysis (e.g., Kieta et al., 2009), the topography of every epoxy mount surface was checked using white light interferometry to ensure a polishing quality that results in less than five microns of topography. Quartz crystals were imaged both in thin sections and epoxy mounts using a panchromatic cathodoluminescence (CL) detector attached to a CamScan MV2300 (W filament) scanning electron microscope (SEM) to characterize the internal structures and to target potential areas of interest for SIMS analysis.

Oxygen-Isotope Analysis by Laser Fluorination

Oxygen-isotope analyses by laser fluorination of quartz phenocrysts and bulk-rock powders were conducted at the stable isotope laboratory at UNIL; for details using the CO₂-laser fluorination at Lausanne, see Lacroix and Vennemann (2015). All bulk-rock powders were treated with 5% HCl prior to analysis to remove carbonate. Sample weights of bulk-rock powders range from 1.1 to 2 mg. Weight of quartz phenocrysts ranged between 0.5–2.2 mg (File S2 [footnote 1]); in some cases, when sufficiently large individual phenocrysts were not available, multiple fragments of quartz (1–3) were used for the analysis. A total of 15 CO₂-laser fluorination analysis sessions conducted for this study include several measurements (3 or 4 out of 12 analyses, per day) of the UNIL in-house quartz standard LS-1 standard during every session (accepted values of δ¹⁸O of 18.1‰). All results were corrected to session value of the LS-1 standard and reported relative to the Vienna standard mean ocean water (VSMOW). Replicate oxygen-isotope analyses of the LS-1 have

an average precision of $\pm 0.1\%$. The average deviation to the accepted value was better than 0.3% . Replicates of whole rocks and minerals have an average precision of $\pm 0.2\%$.

Oxygen-Isotope Analysis by SIMS

Most SIMS $^{18}\text{O}/^{16}\text{O}$ quartz measurements were obtained at the SwissSIMS laboratory at UNIL (14 out of 18 samples), using a Cameca IMS 1280-HR ion probe. The remaining four samples were analyzed using a Cameca IMS 1280 at the WiscSIMS laboratory facility. The measurements followed the description of Kita et al. (2009) with a 10 kV Cs⁺ primary beam and an ~ 2 nA current, resulting in a beam size of ~ 10 μm . A normal incidence electron gun was used to compensate charging on the sample surface; the gun was tuned at the beginning of each session. ^{18}O and ^{16}O were analyzed simultaneously on Faraday cups in multicollection mode with a mass resolution power of ~ 2200 . Faraday cup backgrounds were calibrated at the beginning of each session using the Cameca software. Each analysis consisted of pre-sputtering (~ 30 seconds), automated centering of secondary deflectors (~ 60 seconds), and 16 cycles of 4 seconds counting times. $^{18}\text{O}/^{16}\text{O}$ ratios were normalized relative to VSMOW. To correct for instrumental bias, the primary quartz standard (UNIL-Q1) was used during analyses at both laboratories and has a $\delta^{18}\text{O}$ reference value of $9.8 \pm 0.06\%$ (Seitz et al., 2017). To monitor for potential drift over time during the sessions, two to four unknown analyses were bracketed by at least one analysis of UNIL-Q1. Due to the high density of the primary beam, one session exhibited a mass dependent fractionation of the $^{18}\text{O}/^{16}\text{O}$ ratios within each individual analysis. To correct for this drift, a linear regression was fitted for $^{18}\text{O}/^{16}\text{O}$ ratios versus cycle numbers for each standard analyses. An average slope of all regression from standard analyses was used to correct within spot variations of unknown analyses. Three other sessions exhibited cyclical variations of standard measurements over the course of the 10 h of analyses. These sessions required a drift correction using a 3rd, 4th, and 5th polynomial order, respectively (see File S3 [footnote 1]). Final uncertainty on individual SIMS $\delta^{18}\text{O}$ measurements was computed through the quadratic propagation of internal error (2SE), repeatability of standard analyses used to calibrate the unknown analysis (2SE), uncertainty on the fit at the time of the analysis (95% confidence interval), and the uncertainty on the reference value of UNIL-Q1 (1SD). Typical repeatability (2SD) of UNIL-Q1 analyses was 0.15% – 0.25% (see File S3). For session(s) exhibiting drift over time, the repeatability was 0.4% – 0.5% for all standard measurements before drift correction. Typical final repeatability (2SD) of UNIL-Q1 analyses was 0.20% – 0.35% after drift correction, when needed.

Core and rim regions were selected for spot analysis in each quartz crystal. In some instances, $\delta^{18}\text{O}$ profiles were generated on the SIMS using a higher density of spot analysis within single crystals of selected grains that exhibited significant textural complexity to evaluate the variability (within the possible precision of the 2σ error) of the grains.

SAMPLE DESCRIPTIONS

Sample descriptions are summarized in Table 1. The groundmass has been completely replaced in all ignimbrite samples by secondary minerals (e.g., sericite, chlorite, and clays), which reflect low-temperature hydrothermal alteration. In many cases, the only primary major phase remaining is quartz (Fig. 3). The original phenocryst assemblages were determined using the pseudomorphs in thin sections.

Eastern Andean Margin

We sampled the EQC at four locations along an ~ 230 km transect (Fig. 1B). The three ignimbrite profiles at Lago Posadas, Estancia (Ea.) Ensenada, and at Los Cóndores have several discernable ignimbrites with individual thicknesses ranging from ~ 4 up to 40 m (Figs. 2A–2C). The fourth locality at Lago San Martín includes a single, flat-lying, 3-m-thick ignimbrite.

The ignimbrites of the EQC range in bulk phenocryst concentrations from $\sim 3\%$ – 15% by volume (Table 1). The ignimbrites share a common phenocryst assemblage of quartz, alkali-feldspar, plagioclase, and biotite in decreasing volumetric abundance and accessories of oxides, zircon \pm apatite. Few ignimbrites contained pyroxene (e.g., LPMF3, LCMF1; Table 1). In a few ignimbrite samples, plagioclase is more abundant than quartz (e.g., LPMF6, EEMF10, EEMF8, and LCMF1). Plagioclase phenocrysts are typically completely replaced by sericite. Biotite phenocrysts are often completely altered to chlorite and are only recognizable by its crystal shape. Pumice clasts are small (~ 1 – 3 mm) and represent a small volume of the total bulk tuff (Fig. 3).

The basement metasedimentary units of the Bahía de la Lancha Formation were collected at Lago Posadas and at Ea. Ensenada (closest to Tucu Tucu; Fig. 1B). At Lago Posadas, the lithology sampled is dominated by low-grade metamorphosed graywacke and argillic compositions. The metasedimentary sequence is seen as alternating dark and gray bedding layers (Fig. 2G), which are then overlain by the Jurassic EQC. In thin section, the layered graywackes are strongly folded and composed of alternating layers of quartz and feldspar \pm graphite with layers of muscovite, quartz, and chlorite \pm graphite.

At Ea. Ensenada, pelites (Fig. 2H) and graywackes were collected. In thin section, the pelites are dominated by white mica, chlorite, and quartz. The graywackes contain plagioclase, quartz, white mica, biotite, chlorite, and oxides.

Western Deseado Massif

The eruptive units that comprise the Chon Aike Formation throughout the western Deseado Massif are generally flat-lying and blanket the topography (Figs. 2D and 2F). We sampled four different eruptive units, which include a rhyolitic flow (Deseado Massif rhyolite), the Las Lajas ignimbrite, the La Josefina Dome, and the Cerro Jorge Paz ignimbrite (Fig. 1B).

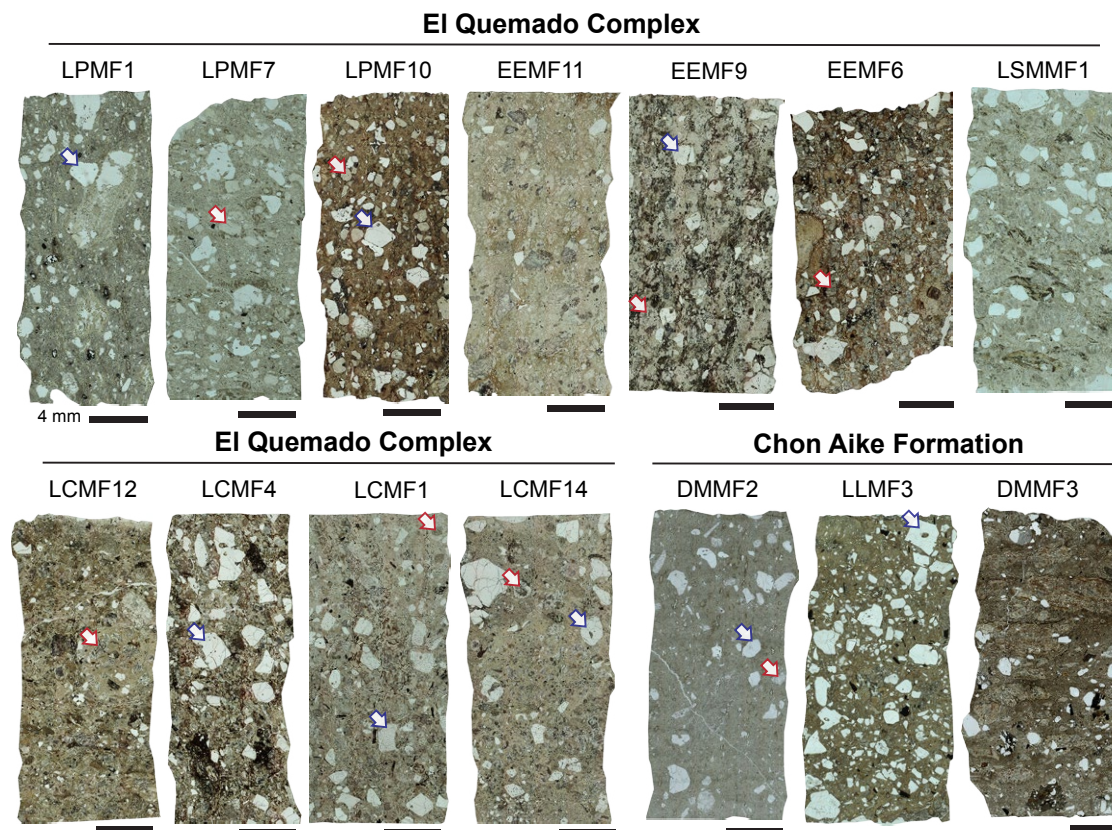


Figure 3. Variability in modal abundances, pumice and lithic content, and matrix color viewed between the El Quemado Complex (ignimbrite) and Chon Aike Formation (ignimbrite and flow) samples, as seen in thin section (plane-polarized light). Blue arrows designate quartz phenocrysts, and red arrows indicate altered feldspars (now sericite). Scale bar is equivalent to 4 mm for all samples.

The westernmost eruptive unit is the Deseado Massif rhyolite, from which we sampled the upper and lower parts of the flow. The rhyolite is phenocryst poor (~5% bulk volume) with only quartz and feldspar observed in thin section (Fig. 3); feldspar has been altered to sericite, and mafic phases were rarely present. Zircon is the only accessory phase present. Both the upper (DMMF1) and lower (DMMF2) portions of the rhyolite flow contain ~1 mm quartz phenocrysts within a white, sugary groundmass. Two generations of quartz were observed macroscopically in DMMF2. One generation was smoky gray, and the second appeared translucent.

The second sample locality is the well-preserved Las Lajas ignimbrite (~50 km³; Echeveste and Fernández, 2012), which is mapped as an ~100-m-thick section, composed of two cooling units. The Lajas ignimbrite is phenocryst rich (~15–18 vol%) and contains abundant quartz, plagioclase, alkali feldspar, biotite and accessories rutile, allanite, zircon, and apatite (Fig. 3). We sampled the lower 30 m of the Las Lajas section, including the basal vitrophyre, the densely welded horizon overlying the vitrophyre, and the poorly welded portion of the section.

The rhyolitic unit at the La Josefina locality is a small dome (area of ~10 km²; Moreira et al., 2010), which was sampled close to the small metasedimentary basement outcrop of the La Modesta Formation. The groundmass of the rhyolite is aphanitic in texture and dark green in color, due to alteration. The primary phenocrysts include quartz, plagioclase, and alkali feldspar with average phenocryst sizes <500 μm.

The eastern-most unit sampled in the Deseado Massif is the moderately welded Cerro Jorge Paz ignimbrite (DMMF3). The ignimbrite lies ~11 km south-east of the La Modesta Formation at the La Josefina locality and is interpreted to be the youngest member of the Chon Aike Formation in the region (Moreira et al., 2009; Moreira et al., 2010). The Cerro Jorge Paz ignimbrite is pumice rich and has quartz and alkali feldspar ~0.5 mm in size, plus biotite and accessories of opaques and zircon.

The metasedimentary basement at the La Josefina locality is the La Modesta Formation (Figs. 1B and 2I). We sampled a variety of the basement rocks, including a muscovite-chlorite schist (LMJMF5), an epidote-quartz calc-silicate

(LMJMF2), and multiple meta-volcanic samples (LMJMF1, LMJMF5, LMJMF6, LMJMF7, and LMJMF8). The muscovite-chlorite schist is dominated by white mica, chlorite, quartz, and interspersed calcite. The calc-silicate sample contains layers rich in calcite with some quartz and chlorite \pm plagioclase. These layers alternate with chlorite, epidote, and quartz zones. The metavolcanics contain a mineralogy of quartz, plagioclase, chlorite, epidote, tremolite, and oxides (rutile); in all sections, carbonate is present in variable proportions.

RESULTS

Bulk-Rock Major- and Trace-Element Compositions

Volcanic Rocks

The volcanic rocks of the EQC and CA plot predominately within the rhyolitic field on the total alkali diagram of SiO_2 wt% versus $\text{Na}_2\text{O} + \text{K}_2\text{O}$ wt%, although three samples of the EQC lie within the dacite field (Fig. 4A). The bulk SiO_2 ranges from ~68 to ~83 wt%. The variability in major-element concentrations in both the EQC and CA is partially related to the effects of secondary alteration in the rock; the highest SiO_2 values of >80 wt% correlate with depletion in Na_2O and CaO wt% (File S1 [footnote 1]). The Zr/Ti versus Nb/Y and Zr/Ti vs Ga discrimination diagrams of Winchester and Floyd (1977) (Figs. 4B and 4C) are less affected by alteration. In this classification, the EQC has a larger proportion of dacitic compositions. However, many of the EQC samples and all of the CA samples remain within the rhyolite field. Most of the data presented here overlap with previously published values for the silicic formations of the CASP (Fig. 4). Additional bivariate plots of major-element concentrations are provided in File S4.

Zr/Hf ranges from 29.2 to 41.6 for the EQC and CA (with one outlier at 50). In general, the CA volcanic rocks plot consistently lower than the EQC, with Zr/Hf values of 28.8–34.1, while most of the EQC values plot within the chondrite field (35–40) (Fig. 5A). Concentrations of Zr versus Hf vary for all units and show a positive linear correlation, with Hf ranging from 2 to 5.5 ppm and Zr ranging from 60 to 230 ppm (Fig. 5B). The values of Eu/Eu^* are similar for all volcanic rocks measured, showing depleted values ranging from 0.12 to 0.25, with >70% of the samples having values of 0.15–0.20 (Fig. 5C). Most of the EQC and the CA have similar Sm/Yb ratios (~1–3.5) with variable La/Sm ratios (~3.2–9.7) (Fig. 5D), although the La Josefina dome (LMJ) is a clear outlier having a much higher Sm/Yb ratio of 8.3–9.4. In general, the EQC tends to have lower La/Sm ratios than the CA, although there is significant variability observed across the four EQC localities (Fig. 5D).

The samples of the EQC and CA plot within the “Volcanic-Arc Granite” field on both tectonic diagrams of Pearce et al. (1984) for Nb versus Y (ppm) and Ta versus Yb (ppm) (Figs. 5D and 5E). The volcanic rocks of the EQC and the Las Lajas ignimbrite overlap in composition (LOG scale), while the concentrations in the three other CA rocks have lower Y and Yb (ppm). Again, the La Josefina dome has lower Y and Yb concentrations (~10–20 ppm and ~1–3 ppm lower, respectively), compared to all other volcanic rocks measured.

The rare-earth element (REE) patterns in the EQC and CA are similar (excluding the LMJ), with enrichments in the light REE (LREE), depletions in the heavy REE (HREE), and a clear Eu anomaly (Fig. 6). The sequence at Lago Posadas shows variability between ignimbrites with similar HREE concentrations but variations in LREE (Fig. 6C), while the Ea. Ensenada section shows the greatest variability in concentrations of LREE and HREE (Fig. 6D). The REE patterns at Los Cóndores are nearly identical for the eight ignimbrites (Fig. 6E). The REE concentrations of Las Lajas and the Cerro Jorge Paz (CJP) ignimbrites are similar to those of the EQC. The DM rhyolite has the lowest REE concentrations. The Josefina dome has a distinct REE pattern where it is much more depleted in HREE.

Paleozoic Basement

Bulk-rock element compositions of representative rocks from the Bahía de la Lancha and the La Modesta Formation are listed in Table 2. The graywackes of the Bahía de la Lancha have SiO_2 contents of 67–85 wt%, while the metapelites have contents from 56 to 63 wt%. The three pelite samples have the highest Al_2O_3 , K_2O , MgO , and Fe_2O_3 wt% of all Bahía de la Lancha samples. The three pelitic rocks at Ea. Ensenada have quite high Ba concentrations (~800–1140 ppm). Sr concentrations are variable, with the lowest concentration of 47 ppm measured in a graywacke (LPMF13) and the highest at 90 ppm in a pelite (EEMF2). Zr concentrations vary from ~160–255 ppm for all units, with the graywacke samples having higher concentrations on average. Hf concentrations are only measurable by XRF in the graywacke samples (having >~3 ppm). Zr/Hf ratios range from 51 to maximum 65.

The calc-silicates and meta-volcanic rocks of the La Modesta Formation are similar in chemical composition, with lower SiO_2 and higher Al_2O_3 , Fe_2O_3 , MgO , and CaO when compared to the muscovite-chlorite schist (Table 2). Ba concentrations are extremely variable for all samples, ranging from 9 ppm to the highest concentration of 530 ppm, both measured in the meta-volcanic rocks. Sr and Zr concentrations vary systematically, with the highest Zr and lowest Sr measured in the muscovite-chlorite schist (185 and 84 ppm, respectively), and the lowest Zr and highest Sr measured in the calc-silicate (67 and 504 ppm, respectively). Hf concentrations were only measured in the calc-silicate and schist, resulting in Zr/Hf ratios of 17 (calc-silicate) and 50 (schist).

CASP Quartz Morphology and Textures

Cathodoluminescence (CL) imaging reveals a range of complex zoning in the magmatic quartz phenocrysts of the ignimbrites and rhyolite lavas (Fig. 7). Quartz crystals are typically large, averaging ~1–2 mm (maximum 3 mm in diameter). Many crystals show evidence of periods of resorption with large embayment features. Some crystals have rounded interior cores that are overgrown by brighter rims. Quartz crystals imaged from different

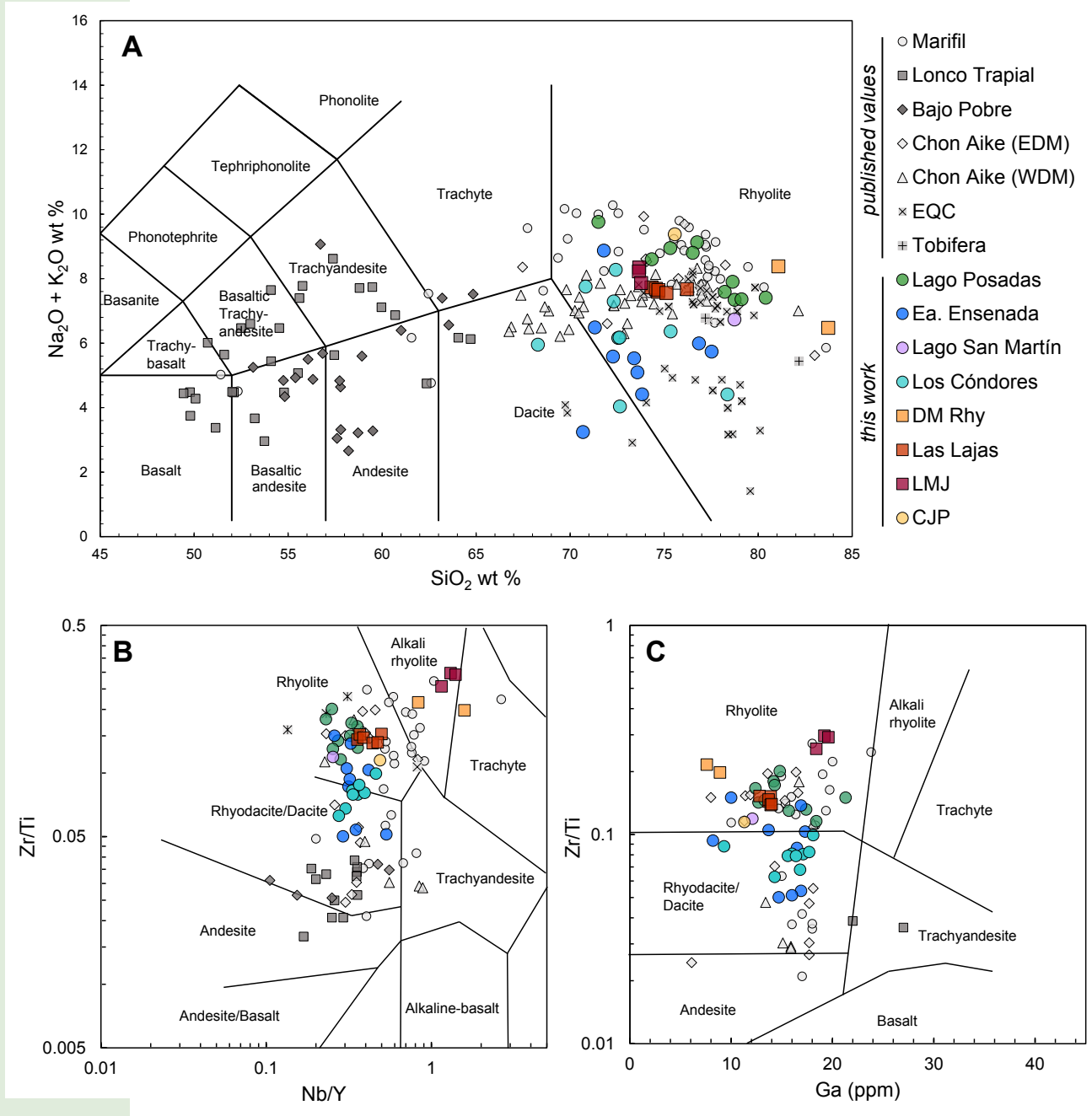


Figure 4. Bulk-rock major-element diagrams. (A) Many of the Chon Aike Silicic Large Igneous Province volcanic units have extremely high bulk SiO₂ wt% (>75 wt%) and variable alkali concentrations due to the widespread, post-emplacement hydrothermal alteration and therefore the majority of the silicic formations plot within the rhyolite field on the total alkali (TAS) diagram. Chon Aike Formation is separated between volcanics erupted in the eastern (EDM) and western Deseado Massif (WDM). More compositions plot within the dacitic field using the discrimination diagrams based on less mobile elements of (B) Nb/Y versus Zr/Ti and (C) Ga (ppm) versus Zr/Ti (after Winchester and Floyd, 1977). References to published values include Gust et al. (1985), Storey and Alabaster (1991), Pankhurst and Rapela (1995), López de Luchi and Rapalini (2002), Guido et al. (2006), Alperin et al. (2007), Márquez et al. (2011), Seitz et al. (2018a), and Navarrete et al. (2019). LMJ—La Josefina Dome; CJP—Cerro Jorge Paz; EQC—El Quemado Complex; Ea.—Estancia; Rhy—rhyolite.

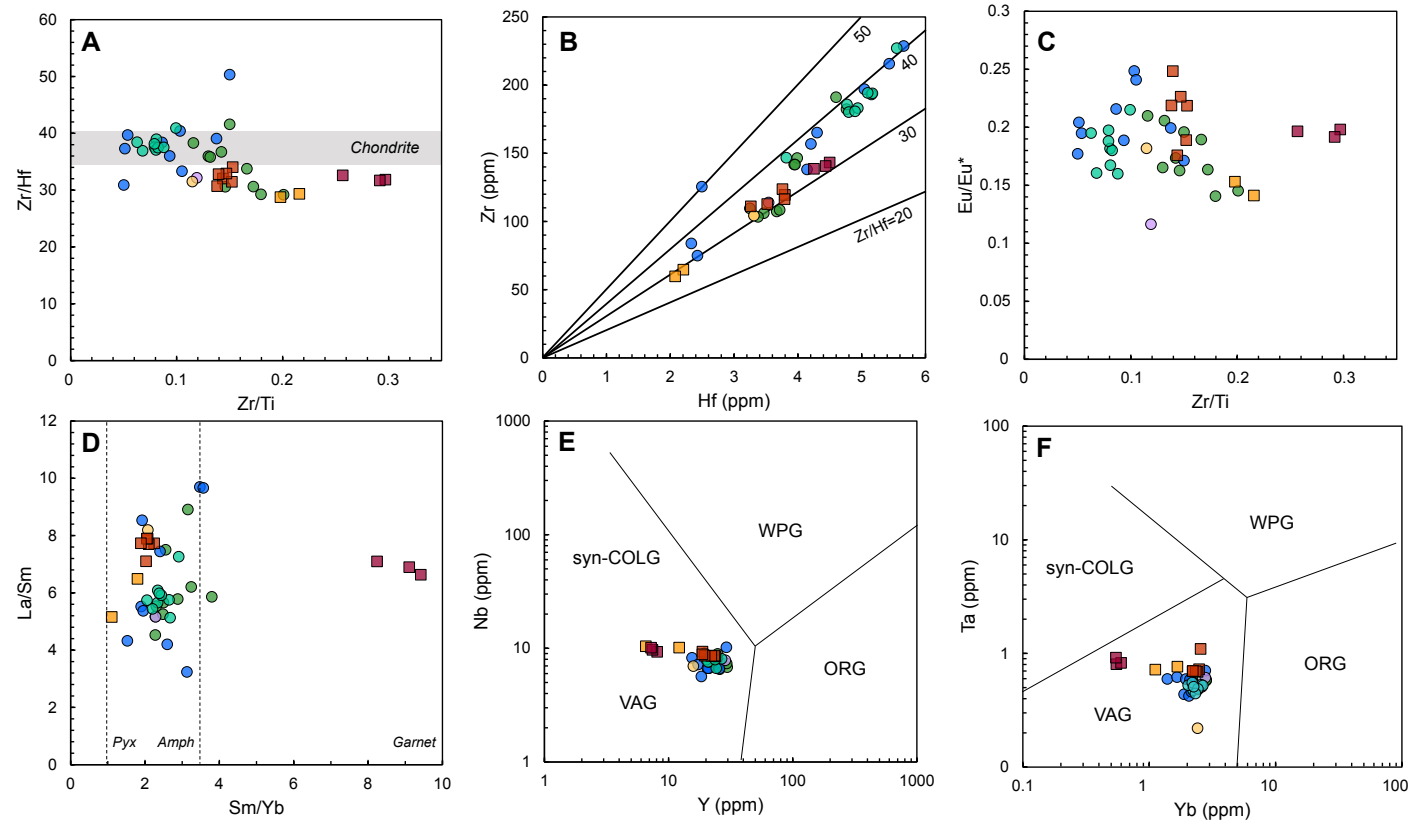


Figure 5. Selected bulk-rock trace elements of the El Quemado Complex (EQC) (ignimbrite) and Chon Aike Formation (CA) volcanic units. Symbols and colors are consistent with Figure 4. (A) The volcanic rocks have relatively consistent Zr/Hf values close to chondritic versus Zr/Ti. (B) Zr (ppm) versus Hf (ppm) concentrations. (C) Eu/Eu* versus Zr/Ti showing source region with extensive feldspar fractionation. (D) La/Sm versus Sm/Yb diagram (Kay et al., 1991) reflecting a magmatic source in the mid- to upper-crust (lower-pressure) stability field of pyroxene (pyx) and amphibole (amph), while the La Josefina dome suggests extraction from a garnet-bearing source (higher pressure). (E) Nb (ppm) versus Y (ppm) and (F) Ta (ppm) versus Yb (ppm) tectonic discrimination diagrams of Pearce et al. (1984) distinguish between syn-collisional granite (syn-COLG), within-plate granite (WPG), volcanic-arc granite (VAG), and ocean ridge granite (ORG) compositions. The EQC and CA volcanic rocks cluster within the VAG field.

ignimbrite samples within a single locality appear to share common CL textures and growth patterns. A comparison between the quartz crystals from different localities reveals widely different growth textures (Fig. 7).

El Quemado Complex

The quartz within the Lago Posadas section is characterized by uninterrupted, fine-scaled oscillatory zonation (Figs. 7A and 7B). Many of the internal structures delineate euhedral, prismatic quartz crystal shapes. Growth zones create a concentric pattern around a single central region.

From the Ea. Ensenada section, quartz samples have typically large, dark cores that are overgrown by brighter rims (Figs. 7C and 7D). The darker cores are often rounded, indicating partial dissolution of the grain. Fine-scaled oscillation is not as apparent as in quartz crystals from other localities (e.g., at Lago Posadas), but subtle oscillatory growth zones within these overall larger zones are present. Quartz melt-inclusions are less abundant in the Ea. Ensenada section and only some crystals show extensive dissolution textures.

The quartz of the single ignimbrite at Lago San Martín presents the most complex CL textures observed for any of the CASP units sampled during this study (Figs. 7E and 7F), and here, the CL texture varies dramatically from crystal to crystal. Complex geometries reflect resorbed zones and fine-scaled oscillations.

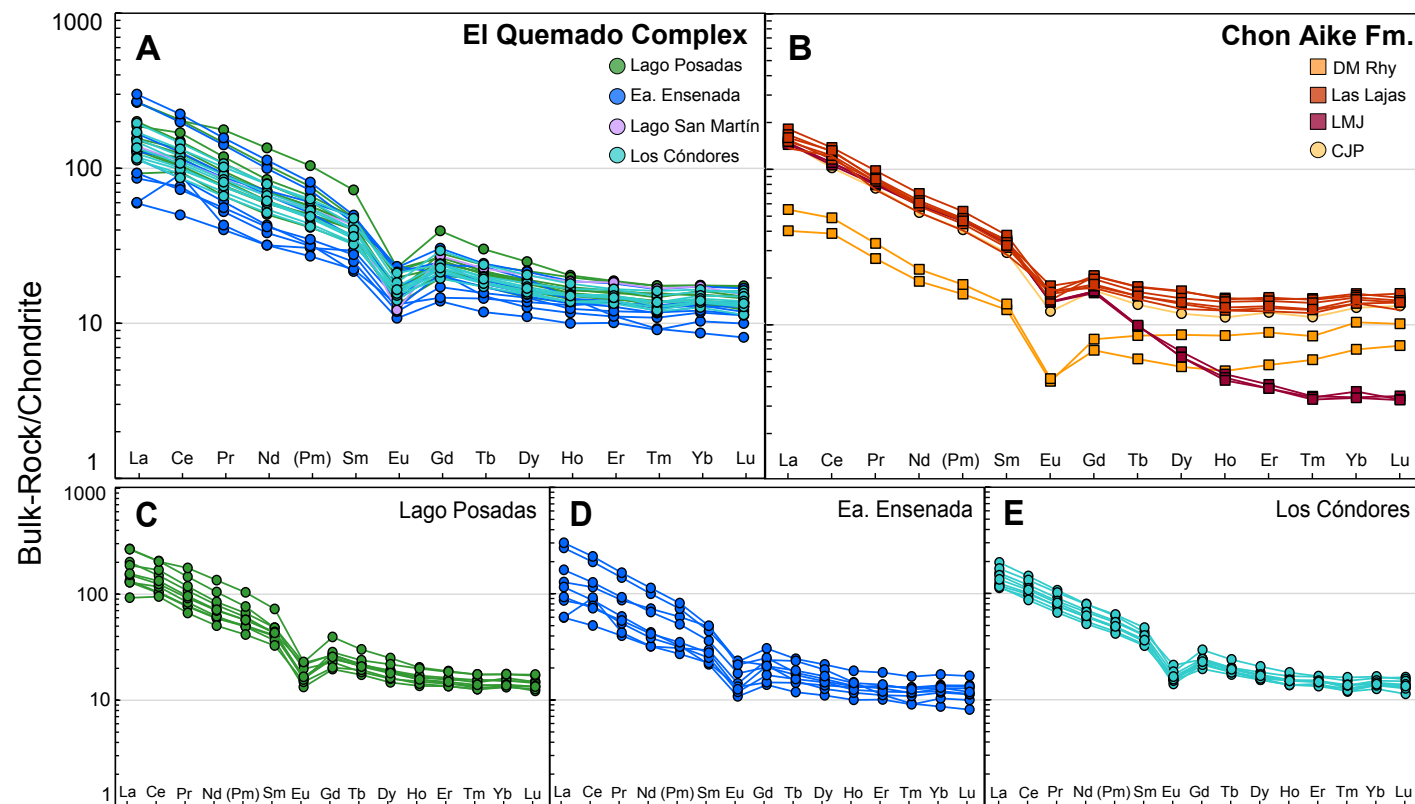


Figure 6. Bulk-rock rare-earth element (REE) concentrations relative to chondrite values of McDonough and Sun (1995) comparing the (A) El Quemado Complex (EQC) and (B) Chon Aike Formation (CA) volcanic rocks. Ignimbrites from the three EQC localities at (C) Lago Posadas, (D) Estancia (Ea.), Ensenada (Tucu Tucu), and (E) Los Cóndores (El Chaltén) are separated to highlight the subtle geochemical differences. REE patterns are similar between the EQC and CA, excluding the La Josefina (LMJ) dome samples which are depleted in heavy REE and are consistent with derivation from a melt extracted from a garnet-bearing source. DM Rhy—Deseado Massif rhyolite; CJP—Cerro Jorge Paz.

The quartz in the ignimbrites of Los Cóndores (El Chaltén) section are similar to those at Lago San Martín in their degree of variability and internal complexities when comparing crystals of the same thin section (Figs. 7G and 7H). In many cases, interior zones are rounded and partially resorbed, followed by younger overgrowths of thick, homogeneous rims. Small-scale, ~1 μm oscillations of dark- and bright-CL zones are less common, but general oscillatory zoning is visible within the bigger zones (Fig. 7H). Melt inclusions are common throughout all CL textural variations of quartz crystals in the Los Cóndores section; dissolution in the form of embayment and significant rounding of the crystals are common. The quartz of Los Cóndores are the largest in average size (up to 3 mm), compared to all other localities sampled in the EQC.

Chon Aike Formation

The magmatic quartz samples from the Chon Aike Formation are concentrically zoned with fine-scaled oscillations (Figs. 7I–7L). The magmatic quartz within the western-most sampled rhyolite (DM rhyolite; Fig. 1B) are often large, sub-euhedral, and have abundant melt inclusions (Figs. 7I and 7J). Large embayments at the surface often connect to interior melt inclusions (Fig. 7I), and CL zones are often truncated by melt inclusions. In addition to the primary magmatic quartz of the DM rhyolite, secondary hydrothermal quartz precipitated in voids. Some quartz nucleated along the void walls and grew into the interior. The nucleated quartz are characterized by euhedral oscillatory zoning that is finer than what is observed in the magmatic

TABLE 2. MAJOR- AND SELECTED TRACE-ELEMENT CONCENTRATIONS AND OXYGEN-ISOTOPE VALUES OF BASEMENT LITHOLOGIES

Lithology	Bahía de la Lancha (Eastern Andean Metamorphic Complex)								La Modesta Formation (Deseado Massif)					
	LPMF11	LPMF12	LPMF13	LPMF14	EEMF1	EEMF2	EEMF13	EEMF14	LMJMF1	LMJMF6A	LMJMF7	LMJMF8	LMJMF2	LMJMF5
Sample														
Rock type	Graywacke	Graywacke	Graywacke	Graywacke	Pelite	Pelite	Pelite	Graywacke	Meta-volcanic	Meta-volcanic	Meta-volcanic	Calc-silicate	Muscovite-chlorite schist	
(wt%)														
SiO ₂	66.67	73.72	84.65	84.57	61.78	55.62	63.48	81.69	48.53	48.69	48.45	50.7	53.62	72.33
TiO ₂	0.82	0.69	0.39	0.37	0.95	1.02	0.88	0.54	1.65	1.68	1.52	1.45	1.03	0.62
Al ₂ O ₃	17.32	14.12	8.35	8.36	20.14	23.52	19.15	8.81	16.21	17.21	16.83	16.69	12.07	13.1
Fe ₂ O ₃ *	7.05	4.37	1.89	2.01	7.62	9.02	7.6	4.13	12.41	10.26	10.61	9.22	6.31	4.86
MnO	0.07	0.05	0.02	0.03	0.08	0.08	0.06	0.04	0.26	0.16	0.16	0.14	0.27	0.08
MgO	2.33	1.51	0.61	0.61	2.46	2.55	2.25	1.11	7.06	8.84	9.86	9.32	4.41	2.18
CaO	0.25	0.39	0.16	0.09	0.18	0.27	0.58	0.52	9.94	9.45	9.69	8.09	19.31	1.4
Na ₂ O	1.93	1.62	2.72	3.15	3.24	3.56	2.0	2.05	3.68	3.45	2.61	4.16	2.79	3.61
K ₂ O	3.37	3.39	1.13	0.74	3.38	4.17	3.83	1.02	0.03	0.04	0.04	0.02	0.06	1.63
P ₂ O ₅	0.19	0.13	0.07	0.06	0.15	0.15	0.15	0.09	0.17	0.15	0.14	0.13	0.11	0.17
Cr ₂ O ₃	0.01	0.01	0	0	0.01	0.02	0.01	0	0.05	0.05	0.06	0.06	0.02	0.01
NiO ₂	0	0	0	0	0.01	0.01	0	0	0.01	0.02	0.03	0.02	0	0
ppm														
Ba	503	720	236	148	1140	1317	797	213	9	217	530	743	21	322
Sr	75	51	47	52	68	90	62	68	290	267	452	269	504	84
Zr	190	237	214	240	164	173	159	254	98	101	92	90	67	185
Hf	3.4	4.4	3.3	4.2	BDL	BDL	BDL	5	BDL	BDL	BDL	BDL	4	3.7
Zr/Hf	56	54	65	57	NA	NA	NA	51	NA	NA	NA	NA	17	50
δ ¹⁸ O (‰ VSMOW)	11.5	12.3	13.6	13.5	12.0	11.3	11.7	14.0	8.9	9.6	8.1	9.5	11.2	11.4

*Fe₂O₃ as total Fe.

Notes: VSMOW—Vienna standard mean ocean water; NA—not applicable; BDL—below detection level.

phenocrysts. Hydrothermal quartz forms coherent clasts with a small grain size (Figs. 7J and 8).

The quartz crystals of the Las Lajas ignimbrite show fine-scaled magmatic oscillations and commonly have melt inclusions (Figs. 7K and 7L), similar to the DM rhyolite. Some crystals have thick, bright-CL rims that overgrow a partially resorbed darker interior. Many crystals are subhedral and partially resorbed.

The quartz samples of the Cerro Jorge Paz ignimbrite (DMMF3) and the Josefina Dome are significantly smaller than those of all the other CASP samples from this study. The CJP have quartz sizes maximum of ~500 μm in diameter; the quartz phenocrysts of the Josefina dome are the smallest size observed at ~200–300 μm. Quartz in the Josefina Dome are generally scarce in thin section; however, like the other CA samples, the quartz CL texture predominately exhibits simple, fine-scaled magmatic oscillations (see also File S5 [footnote 1]).

Oxygen-Isotope Composition of CASP Quartz as Determined by SIMS

Eighteen volcanic samples were selected for oxygen-isotope analysis by SIMS, with a total of 540 analyses from 125 individual quartz phenocrysts. The results

are combined to test for variability between the EQC and CA Formations (Table 3), excluding the LMJMF3 and LMJMF10 samples, where only fragments were analyzed. The quartz phenocrysts are representative of the sample population for each ignimbrite and/or rhyolite and for each sample locality based on similarity to the CL patterns observed in thin section (File S5). Common for all igneous quartz phenocrysts is that they do not show any significant oxygen-isotope zoning, even in samples with multiple dissolution features and complex CL zoning.

El Quemado Complex

Quartz δ¹⁸O values measured in the EQC range from 9.6‰ to 12.3‰. At the northern-most locality, the three ignimbrites at Lago Posadas have the lowest δ¹⁸O value (9.6‰–10.9‰) (Fig. 9). There is no significant change from the lower-most ignimbrite unit (LPMF10) to the top of the sequence (LPMF1) at Lago Posadas (Table 3).

The ignimbrite profile at Ea. Ensenada has the largest variation in δ¹⁸O values of all localities within the EQC measured in this study. There is a decrease in δ¹⁸O values from the basal ignimbrite (11.3‰–12.3‰) toward the uppermost

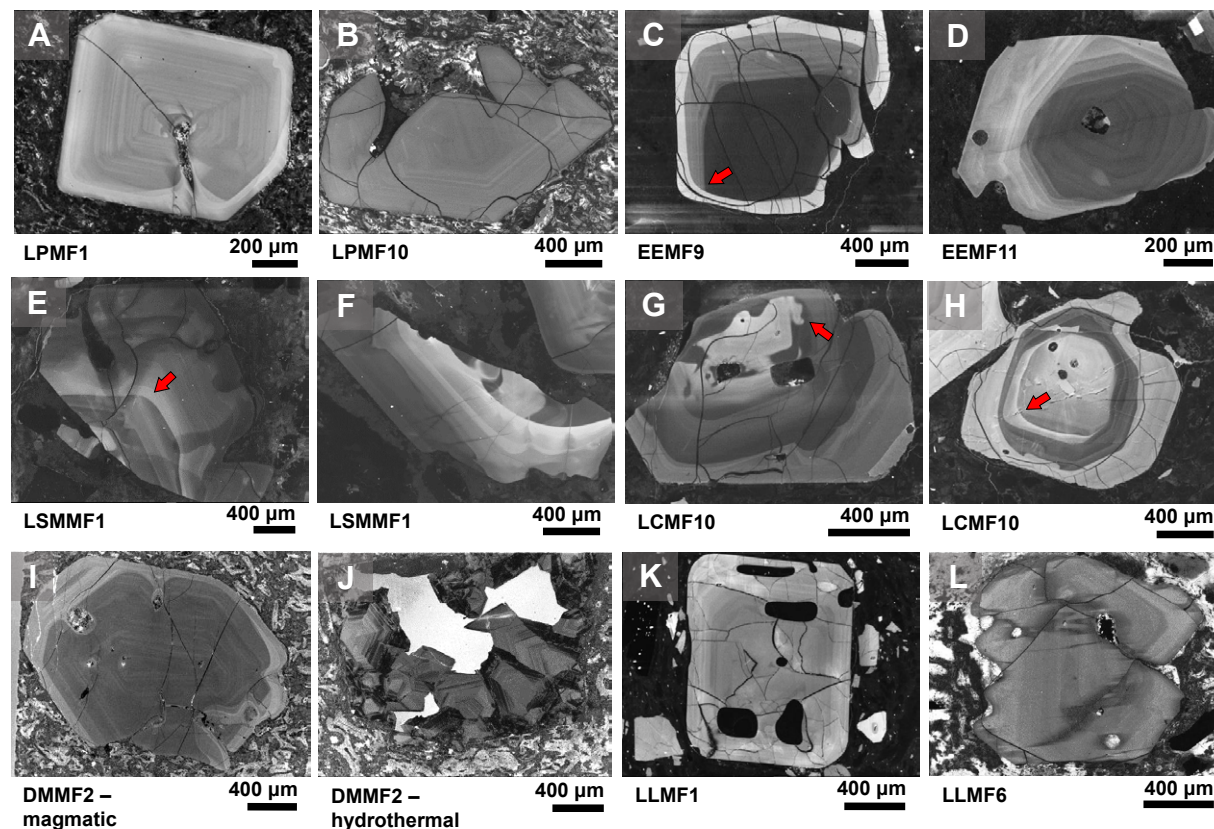


Figure 7. Characteristic quartz cathodoluminescent (CL) textures seen in thin section for the Chon Aike Silicic Large Igneous Province volcanic rocks. CL imaging reveals a range of often complex zoning in the magmatic quartz phenocrysts. Red arrows point to internal dissolution surfaces. (A–H) In the El Quemado Complex, CL textural complexity increases toward the south, with the most complex textures shown at (G and H) Los Cóndores. (I–L) In comparison, the Chon Aike Formation quartz mostly exhibit oscillatory growth. (I and J) Both generations of quartz are shown from the Deseado Massif Rhyolite sample.

ignimbrite (9.7‰–10.4‰; although, a bimodality exists within EEM10 with two phenocrysts having high $\delta^{18}\text{O}$ values, ranging from 11.5‰ to 11.9‰) (Fig. 9). Only one grain shows a clear increase from the core to rim (EEMF6-quartz 5; Fig. 10), increasing from 11.4‰ to 12.2‰ at the outermost rim.

Because of the complexity of the CL patterns revealed in the quartz of the Lago San Martín ignimbrite (Figs. 7E–7F), we increased the number of analyses to test for variability relating to textures. From ten individual quartz phenocrysts and 99 measurements, the $\delta^{18}\text{O}$ of LSMMF1 ranges from 10.5‰ to 11.6‰ (Fig. 9).

The quartz of Los Cóndores (El Chaltén) measured for four ignimbrites are extremely similar in their oxygen-isotope composition (Fig. 9). The lower three ignimbrites have nearly the same range of values from 10.6‰ to 11.4‰ (Table 3).

The uppermost ignimbrite (LCMF12) has a slightly larger $\delta^{18}\text{O}$ range with 10.4‰–11.6‰ (average 11.1‰), although only a single quartz phenocryst was measured with the lowest $\delta^{18}\text{O}$ values of 10.4‰ and 10.7‰ (File S5 [footnote 1]). The values are plotted against those of Seitz et al. (2018a)—comparing the ignimbrite profile of Cerro Polo (10.5‰–11.5‰) and those of the rhyolite domes (11.0‰–13.7‰) (Fig. 9).

Chon Aike Formation

SIMS analyses of quartz for the four silicic units sampled from the Chon Aike Formation from the western portion of the Deseado Massif region are

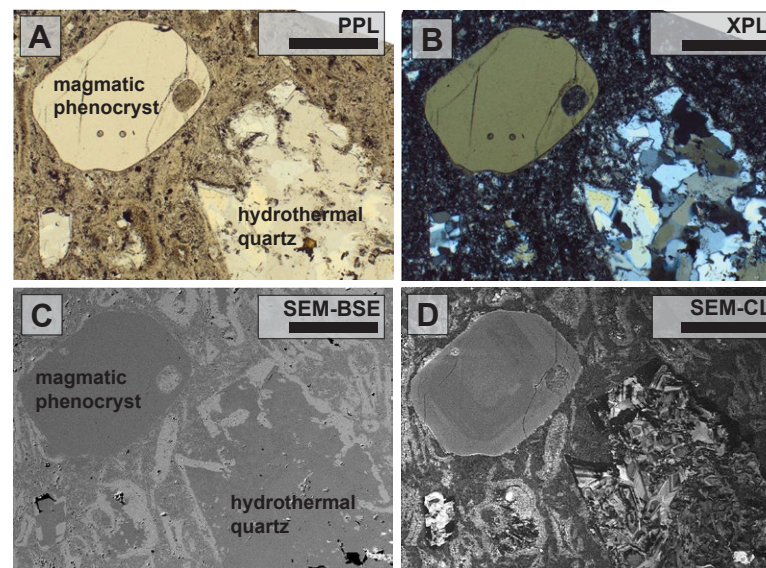


Figure 8. (A–D) Microscopic images showing the close proximity between the two quartz generations in the Deseado Massif Rhyolite (DMMF2), with the scale bar corresponding to 500 µm in all images. Although the bulk rock experienced heavy alteration, the magmatic quartz shows no indication of alteration. Microscopic images using (A) plane-polarized light (PPL); (B) cross-polarized light (XPL); (C) scanning electron microscopy (SEM)–backscatter electrons (BSE); and (D) SEM-cathodoluminescence (CL); CL imaging reveals the characteristic CL patterns of the two quartz generations.

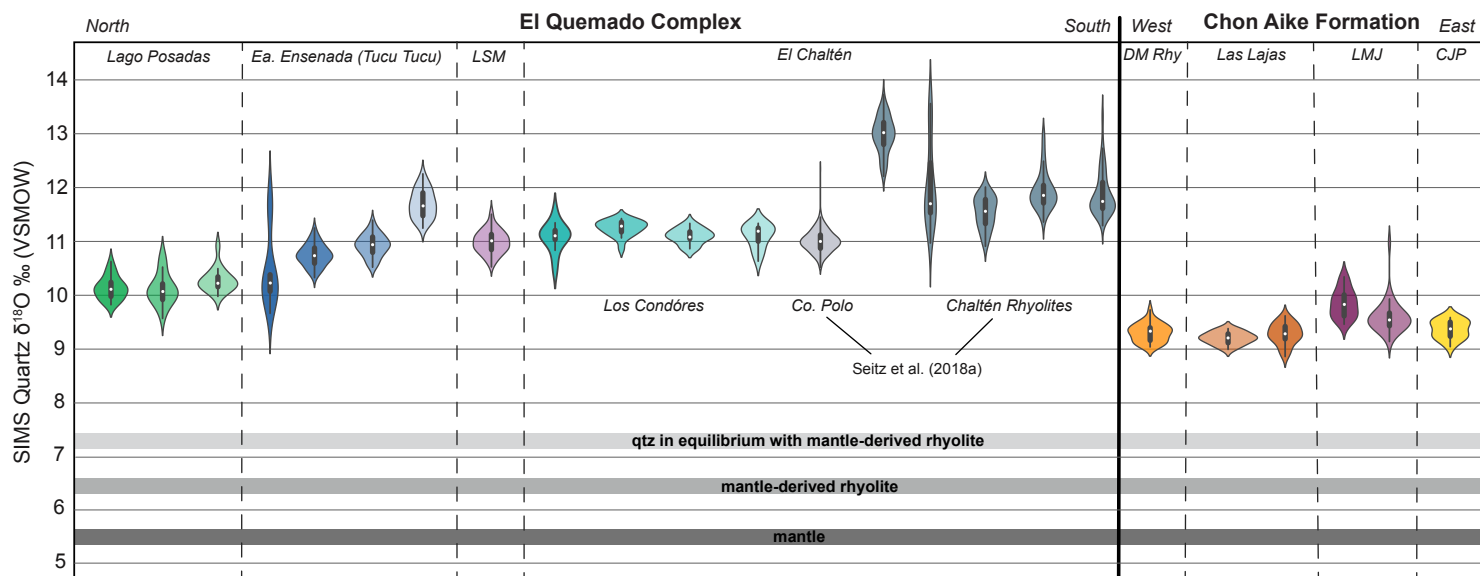


Figure 9. Violin plot of magmatic quartz secondary ion mass spectrometry (SIMS) $\delta^{18}\text{O}$ measurements for 14 volcanic units from the El Quemado Complex (EQC) and Chon Aike Formation. EQC samples measured from an ignimbrite sequence at a single location are also arranged from top to bottom, from left to right. Published EQC quartz $\delta^{18}\text{O}$ measurements from the El Chaltén region (Seitz et al., 2018a) are plotted for the regional comparison. All oxygen-isotope values are elevated relative to quartz values in equilibrium with a rhyolite derived by closed-system fractionation from a mantle-derived source ($\Delta_{\text{quartz-melt}} = 0.6$). qtz—quartz; DM Rhy—Deseado Massif Rhyolite; LMJ—La Josefina Done; CJP—Cerro Jorge Paz; LSM—Lago San Martín.

TABLE 3. SUMMARY OF BULK-ROCK AND QUARTZ OXYGEN-ISOTOPE VALUES BY LASER FLUORINATION AND SIMS SEPARATED BY SAMPLE AND LOCALITY

Sample	Ign/Rhy	Laser fluorination		SIMS			
		Whole-rock $\delta^{18}\text{O}$ (‰)	Quartz $\delta^{18}\text{O}$ (‰)	Average quartz $\delta^{18}\text{O}$ (‰)	Median quartz $\delta^{18}\text{O}$ (‰)	Number of quartz samples	Number of analyses
Lago Posadas							
LPMF1	Ign A	14.8	10.0	10.1	10.1	10	22
LPMF2	Ign A	18.5 [†]	–	–	–	–	–
LPMF3	Ign B	15	9.9	–	–	–	–
LPMF4	Ign C	14.3	10.3	–	–	–	–
LPMF5	Ign D	16.5	9.8	–	–	–	–
LPMF6	Ign E	14.3	10.0	–	–	–	–
LPMF7	Ign F	15.5	9.5	10.1	10.1	7	23
LPMF8	Ign F	16.2	10.2	–	–	–	–
LPMF9	Ign F	13.7	10.1	–	–	–	–
LPMF10	Ign G	13.2	9.7	10.3	10.2	8	16
Estancia Ensenada (Tucu Tucu)							
EEMF10	Ign A	15.9	11.2	10.5	10.2	6	22
EEMF11	Ign B	16.4	11.8	10.7	10.7	8	53
EEMF12	Ign B	16.1	10.4	–	–	–	–
EEMF7	Ign C	14.2	11.0	–	–	–	–
EEMF8	Ign D	13.1	10.6	–	–	–	–
EEMF9	Ign E	14.1	11.7	10.9	10.9	11	56
EEMF6	Ign F	14.4	11.7 [†]	11.7	11.6	9	39
EEMF4	Ign G	13.7	11.3	–	–	–	–
Lago San Martín							
LSMMF1	Ign	15.0	11 [†]	11	11	10	99
Los Cóndores (El Chaltén)							
LCMF12	Ign A	14.9	11.4	11.1	11.1	6	15
LCMF11	Ign B	14.7	11.2	–	–	–	–
LCMF8	Ign C	13.2	11.2 [†]	–	–	–	–
LCMF7	Ign C	13.3 [†]	11.2	–	–	–	–
LCMF10	Ign D	13.7	11.1	–	–	–	–
LCMF6	Ign E	13.3	11.3	–	–	–	–
LCMF4	Ign F	13.4	10.9	11.3	11.3	6	17
LCMF1	Ign G	14.7	11.1	11.1	11.1	6	15
LCMF14	Ign H	12.5 [†]	11.0	11.1	11.2	5	13
Deseado Massif (undifferentiated Chon Aike Formation)							
DMMF1	Rhy	9.9	9.3	–	–	–	–
DMMF2	Rhy	5.5	2.3/9.3*	4.2/9.3*	4.3/9.3*	10	32
Las Lajas Ignimbrite							
LLMF1	Vitrophyre	12.9 [†]	9.5 [§]	–	–	–	–
LLMF3	Densely welded	9.4	8.8 [†]	9.2	9.2	12	16
LLMF6	Poorly welded	9.4	8.9	9.3	9.3	7	30
La Josefina Dome							
LMJMF3	Rhy	7.5 [†]	NA	9.9	9.8	NA	23
LMFMF9	Rhy	7.3	NA	–	–	–	–
LMFMF10	Rhy	12.1	NA	9.6	9.6	NA	34
Cerro Jorge Paz Ignimbrite							
DMMF3	Ign	12.1	NA	9.4	9.4	4	15

Notes: All values are referenced to Vienna standard mean ocean water (VSMOW). SIMS—secondary ion mass spectrometry; Rhy—rhyolite; Ign—ignimbrite; NA—not applicable. Dashes denote unanalyzed samples.

*Denotes the two populations in the Deseado Massif rhyolite: hydrothermal and/or magmatic values.

[†]Duplicated analyses.

[§]Average of four analyses.

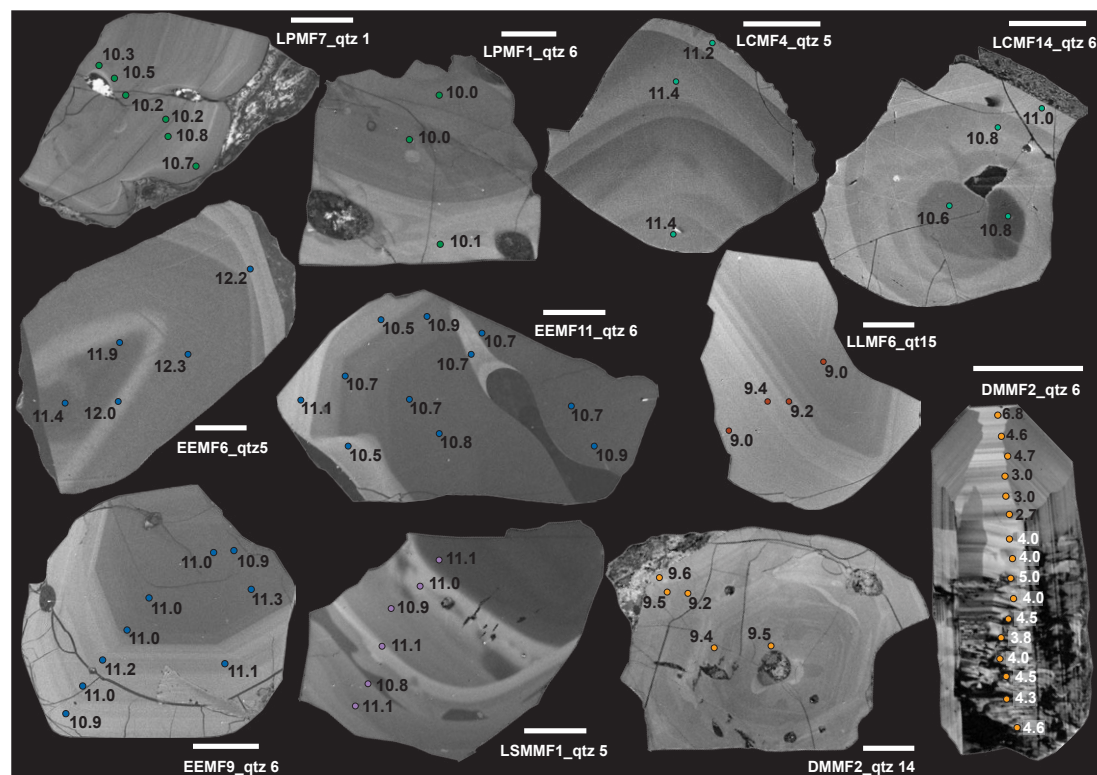


Figure 10. Representative secondary ion mass spectroscopy (SIMS) spot analysis of oxygen isotope values in quartz ($\delta^{18}\text{O}$ ‰, corrected to Vienna standard mean ocean water). $\delta^{18}\text{O}$ values show no systematic variation with changing cathodoluminescent intensities; most phenocrysts have homogeneous oxygen isotope values. Phenocrysts with adhered matrix were selected to ensure rim measurements are recording the final $\delta^{18}\text{O}$ value of the pre-eruptive melt. Error bar for each phenocryst represents 200 μm . The error associated with each spot analysis is presented in the File S3 (text footnote 1).

remarkably homogeneous (Fig. 9). The quartz of the DM rhyolite, Las Lajas ignimbrite, and the Cerro Jorge Paz ignimbrite have a nearly identical oxygen-isotope composition, ranging from 9.1‰ to 9.7‰ (DMMF2), 9.0‰–9.6‰ (LLMF3 and LLMF6), and 9.1‰–9.6‰ (DMMF3), respectively. Similar to those of the EQC, no changes in oxygen-isotope composition were observed from core to rim in any of the 33 quartz phenocrysts.

The quartz measured in the La Josefina dome are slightly higher in $\delta^{18}\text{O}$ composition, ranging from 9.2‰ to 10.4‰ for both samples (LMJMF3 and LMJMF10), with one anomalously high value of 11.0‰ measured in a single quartz fragment (LMJMF10-quartz 5; File S5).

In addition to the primary magmatic quartz phenocryst, a single secondary hydrothermal quartz generation was measured for its oxygen-isotope composition with SIMS. Between the two quartz generations of the Deseado Massif rhyolite, the secondary hydrothermal quartz records lower $\delta^{18}\text{O}$ values, ranging from 2.7‰ to 6.8‰ across a 15-spot profile along the longest axis of the polished crystal face (Fig. 10). These values are much lower than the average $\delta^{18}\text{O}$ values of 9.3‰ in the magmatic quartz phenocrysts.

Oxygen-Isotope Composition of CASP Quartz as Determined by Laser Fluorination

A total of 45 individual phenocrysts separated from 33 volcanic samples and 58 bulk-rock (37 volcanic and 14 basement rocks) were analyzed by laser fluorination. A summary of the results is presented in Figure 12 and Tables 2 and 3.

El Quemado Complex Quartz

Oxygen-isotope values measured in quartz by laser fluorination are consistent with those measured by SIMS. Values for the EQC range from 9.5‰ to 11.9‰, with a trend of increasing values toward the south. For the Lago Posadas and Los Cóncores ignimbrite sequences, there is no correlation between its $\delta^{18}\text{O}$ value and its sequence in stratigraphy. The ignimbrite sequence at Ea. Ensenada exhibited the greatest variability in quartz oxygen isotopes for all conformable sections sampled in the EQC (Fig. 11). Quartz at Ea. Ensenada

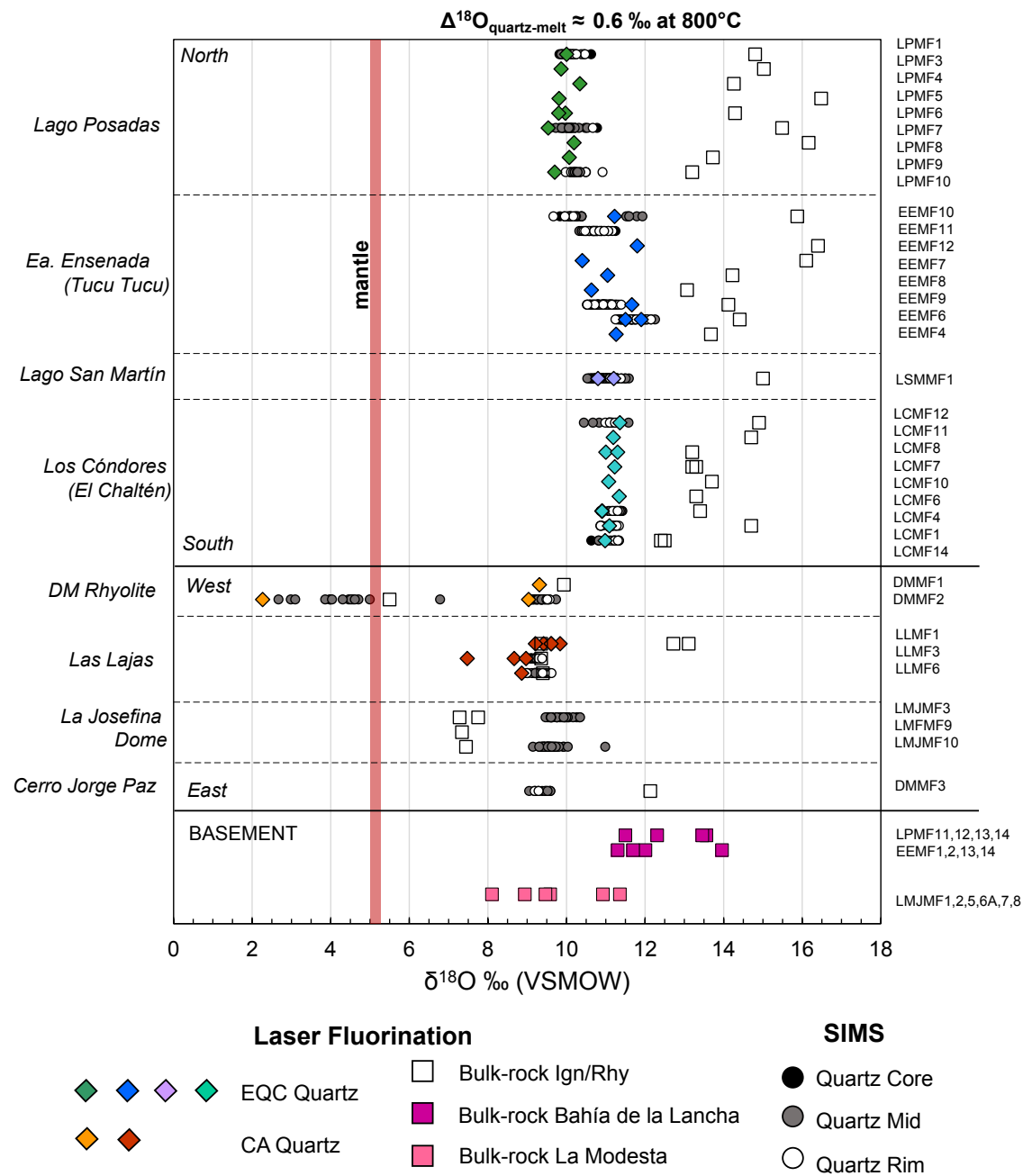


Figure 11. Summary of oxygen isotope measurements by laser fluorination and secondary ion mass spectroscopy (SIMS) for the El Quemado Complex (EQC) and Chon Aike Formation (CA). All magmatic quartz values are elevated relative to the primitive mantle value of 5.5 ‰. SIMS measurements in quartz are separated by positioning on the crystal (core, mid, rim). Bulk rock samples of basement units are separated by location, but multiple samples from the same location are overlain on the same horizon; values per sample are indicated in Table 2. Ea. – Estancia; Ign/Rhy – ignimbrite/rhyolite; VSMOW – Vienna standard mean ocean water.

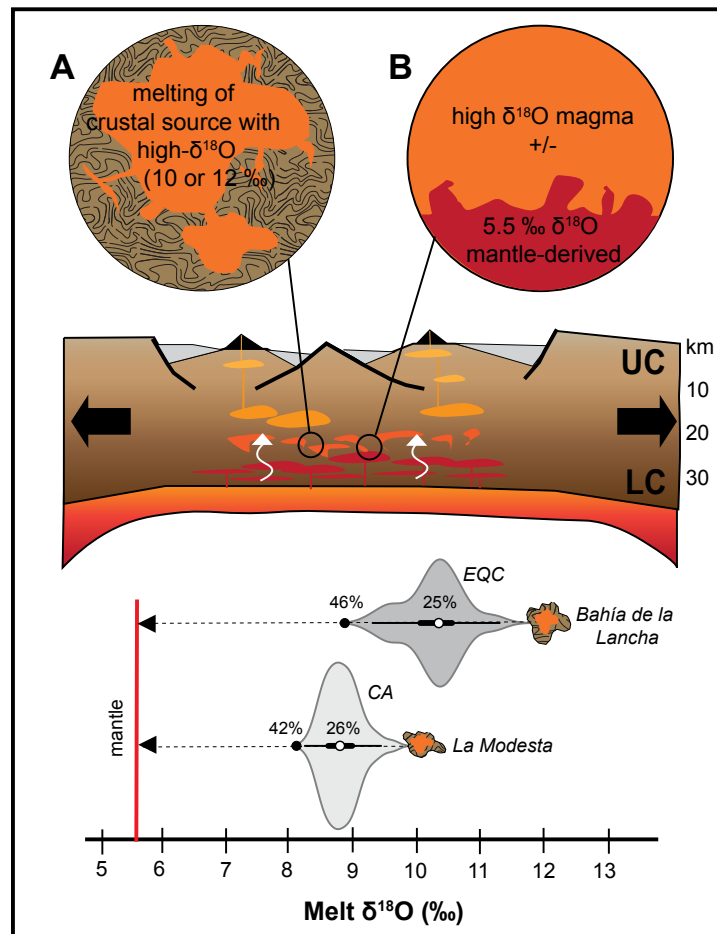


Figure 12. Generation of silicic magma via crustal anatexis in the mid to lower crust (LC) within an extensional setting. Violin plots are constructed using the total range of melt $\delta^{18}\text{O}$ values measured in the El Quemado Complex (EQC) (dark gray) and the Chon Aike Formation (CA) (light gray). Dashed line indicates the evolution between 0–100% mixing with a primitive mantle source, with the arrow pointing toward increasing mantle mixing. (A) The generation of large volumes of widespread, high $\delta^{18}\text{O}$ magmas is generated via bulk melting of an elevated (10 or 12 ‰ $\delta^{18}\text{O}$) crustal source enriched in heavy oxygen. (B) Melt values lower than the starting material could reflect heterogeneity in the crustal source and/or involvement with the mantle. Maximum mantle involvement for both EQC and CA is <50% to generate the lowest melt values observed, while average melt values require ~25% mantle contribution (calculated average and median values are identical for the EQC and CA). UC—upper crust.

trend toward lower $\delta^{18}\text{O}$ values with increasing stratigraphy; however, values measured by laser fluorination versus SIMS deviate in the uppermost two ignimbrite units (Fig. 11).

Chon Aike Formation Quartz

The quartz phenocrysts in the CA range from 8.7‰ to 9.8‰ for the DM rhyolite samples and the Las Lajas ignimbrite, with one outlier value of 7.5‰ (LLMF6). No single quartz crystals were analyzed via laser fluorination from the LMJ rhyolitic dome, due to the small size of quartz phenocrysts.

The lower portion of the DM rhyolite flow (DMMF2) has two visible quartz populations in hand sample that gave a value of 2.3‰ for a clear quartz and 9.0‰ for the smoky-gray variety (Fig. 11). The $\delta^{18}\text{O}$ values of each quartz population of DMMF2 correspond well with SIMS data.

Oxygen-Isotope Composition of Bulk Rock as Determined by Laser Fluorination

Volcanic Bulk Rock

All ignimbrite samples measured in the EQC have elevated bulk-rock $\delta^{18}\text{O}$ values, ranging from 12.4‰ to 18.7‰ (Fig. 11). In comparison, the bulk-rock $\delta^{18}\text{O}$ values in the CA are extremely variable per each sample. The two bulk-rock $\delta^{18}\text{O}$ values of the DM rhyolite are extremely different—DMM1 is similar to the bulk quartz value at 9.9‰, while the bulk-rock value of the DMMF2 is intermediate to the two quartz values at 5.5‰ (Fig. 11).

In the Las Lajas ignimbrite, the bulk-rock value for the vitrophyre is the highest in $\delta^{18}\text{O}$ for the Las Lajas ignimbrite at 12.9‰ ($n = 2$), while the bulk-rock values from the other two horizons in the ignimbrite section are closer to the average quartz value of the ignimbrite (9.4‰). All three of the LMJ rhyolite samples have lower bulk-rock $\delta^{18}\text{O}$ values when compared to their quartz values, ranging from 7.3‰ to 7.5‰ (Fig. 11). Lastly, the CJP ignimbrite has an elevated bulk-rock $\delta^{18}\text{O}$ value of 12.1‰.

Paleozoic Basement Bulk Rock

At the Lago Posadas locality, the two compositionally similar graywacke compositions in the Bahía de la Lancha have the highest bulk-rock values of 13.5‰ and 13.6‰ (LPMF13 and LPMF14) (Table 2). The two layered graywacke rocks are lower in $\delta^{18}\text{O}$ composition with values of 11.5‰ and 12.3‰ (LPMF11 and LPMF12).

The two pelites from Ea. Ensenada yielded $\delta^{18}\text{O}$ values of 11.7‰ and 12.0‰, while the $\delta^{18}\text{O}$ of the two graywackes are 11.3‰ and 14.0‰. The sample EEMF14, which is compositionally similar in major and trace elements (e.g., Ba, Sr,

and Zr ppm) to the graywackes at Lago Posados (LPMF13 and LPMF14), is also isotopically similar with a $\delta^{18}\text{O}$ of 14.0‰, compared to the Lago Posados samples (13.5‰ and 13.6‰).

The basement rocks from the La Modesta Formation analyzed for bulk-rock oxygen isotopes include the calc-silicate (11.2‰), the muscovite-chlorite schist (11.4‰), and the multiple meta-volcanic rocks, which systematically have the lowest bulk-rock oxygen-isotope value when compared to all basement rocks analyzed (8.1‰, 8.9‰, 9.5‰, and 9.6‰) (Table 2).

■ DISCUSSION

Retention of Magmatic Quartz $\delta^{18}\text{O}$ Values

The chemical and isotopic composition of volcanic rocks can be changed significantly by hydrothermal alteration. Therefore, minerals with a low susceptibility to alteration give better indications of the original coexisting melt $\delta^{18}\text{O}$ value than bulk rock (Taylor, 1974; Muehlenbachs, 1986; Feeley et al., 2008; Bucholz et al., 2017). While quartz is easily recrystallized in stressed environments (e.g., Passchier and Trouw, 1998), quartz is resistant to dissolution in static environments, due to its slow dissolution kinetics (Lasaga, 1995). Nevertheless, before quartz can be used with confidence to identify magmatic isotopic compositions, the importance of diffusion needs to be evaluated to exclude late, post-eruption alteration of quartz oxygen-isotope compositions.

The $\delta^{18}\text{O}$ fractionation between melt and quartz at igneous temperatures is \sim 0.6‰, with higher values in quartz (Bindeman et al., 2004). Figure 11 shows oxygen-isotope data for coexisting quartz phenocrysts and bulk rock, where in all but three cases, the bulk-rock compositions are higher than that of the quartz. Since all rock matrices are heavily hydrothermally altered, we attribute this reverse fractionation to hydrothermal water-rock interaction, which increased the whole-rock composition (e.g., $\Delta^{18}\text{O}_{\text{clay-H}_2\text{O}} > 10\text{‰}$ at 150 °C; Savin and Epstein, 1970). Indeed, the high bulk-rock $\delta^{18}\text{O}$ values of 12.4‰–16.5‰ are correlated to alteration of the matrix and the replacement of primary feldspar and biotite phases into hydrothermal minerals including sericite, epidote, and calcite. Diffusion is slow within intact quartz phenocrysts at these low temperatures ($2.8 \times 10^{-28} \text{ m}^2\text{s}^{-1}$ at 250 °C; Sharp et al., 1991). This is well demonstrated by the fact that in the quartz $\delta^{18}\text{O}$ values do not show any intra-crystalline isotope disturbances at the boundary of the 125 individual quartz phenocrysts measured by SIMS ($n = 536$ analyses). Hence, we interpret the isotopic composition of quartz phenocrysts to reflect the primary magmatic compositions before eruption.

In comparison, the thermal conditions of the hydrothermal alteration in the volcanic rocks in the Deseado Massif are more variable, since a shift in bulk-rock $\delta^{18}\text{O}$ toward lower and higher values is observed (Fig. 11). In one case, we identified hydrothermal quartz likely growing in cavities in the Deseado Massif rhyolite (DMMF2). Its low $\delta^{18}\text{O}$ values ranging between 2.7‰ and 6.7‰ (Fig. 10) indicate interaction with meteoric waters, most likely during high-temperature

(>500 °C) hydrothermal alteration. But even in this case, the magmatic quartz phenocrysts in the same sample maintain their high oxygen-isotope values of \sim 9.5‰, with no indication of the presence of diffusive exchange rims. In fact, the oxygen-isotope composition of the igneous quartz is the same as those of proximal CA volcanic rocks (Fig. 10).

The widespread homogeneity of high $\delta^{18}\text{O}$ quartz phenocrysts is particularly striking when compared to the complex CL patterns observed, which indicate in some cases multiple dissolution-regrowth events as well as oscillatory zoning during a growth period (Figs. 7 and 10). Major changes in quartz CL intensities are interpreted to correlate with concentrations of trace elements (e.g., Ti and Al; Seitz et al., 2016). Dissolution-regrowth cycles are typically interpreted to reflect changes in physical (pressure and/or temperature) or chemical (magma mixing or replenishing events), while oscillatory zoning has been interpreted to reflect with the same external forcing as discussed before (e.g., P , T , X) or due to internal forcing due to feedbacks in disequilibrium growth (Wark and Watson, 2006; Gualda and Sutton, 2016; Pamukcu et al., 2016; Seitz et al., 2016).

The differences in oxygen-isotope and CL zoning variations need to be further discussed, since two calibrations of Ti diffusivity can be found in the literature. In the first calibration, both the intra-crystalline self-diffusivities of titanium and oxygen within quartz are very similar, at the same magmatic temperature: $4.4 \times 10^{-19} \text{ m}^2\text{s}^{-1}$ (Cherniak et al., 2007) compared to $6.3 \times 10^{-19} \text{ m}^2\text{s}^{-1}$ (Sharp et al., 1991), for titanium and oxygen, respectively at 1000 °C. In this case, oxygen and Ti behave similarly, and hence oxygen composition of the magma during quartz growth did not vary in the magma. Alternatively, the new Ti-in-quartz diffusion coefficient of Jollands et al. (2020) yields a slower diffusivity for titanium in quartz by two to three orders of magnitude (e.g., $8.8 \times 10^{-22} \text{ m}^2\text{s}^{-1}$ at 1000 °C). If the Ti-diffusion in quartz is significantly slower than that of oxygen, fine-scale oscillations can be preserved, while homogenizing the isotopic composition of quartz in a prolonged residence time in the magma chamber such that oxygen would reflect the composition of the magma before eruption, but the history of isotope variations during quartz growth would be erased. However, to achieve oxygen-isotope equilibrium between the melt and the quartz crystal requires that the quartz was held at high temperature for sufficiently long periods of time (e.g., \sim 100 k.y. at 800 °C, over 500 μm ; fig. 13 of Seitz et al., 2018a). Thus, if the $\delta^{18}\text{O}$ was effectively re-homogenized in the quartz, the value measured reflects the final melt composition, prior to eruption.

In either case, all igneous $\delta^{18}\text{O}$ values of the EQC and CA quartz are original magmatic signatures and reflect the composition of the hosting melt in the period of quartz crystal growth. In the following discussions, we restrict our discussion of $\delta^{18}\text{O}$ values only to phenocrystic quartz.

Origin of High $\delta^{18}\text{O}$ Silicic Magmas

The isotope ratios of oxygen in magmas are difficult to change by closed-system fractionation processes at temperatures for silicic magmas (\sim 700–900 °C). The generation of a rhyolite (>70 wt% SiO_2) by closed system fractionation from

a mafic source (~55 wt% bulk SiO₂) causes less than one permil increase in δ¹⁸O for ~20 wt% changing SiO₂ (Valley, 2003; Bindeman et al., 2004; Bindeman, 2008). Therefore, a rhyolite melt derived purely from fractional crystallization of mantle-derived mafic melt with a δ¹⁸O of 5.5‰ would result in a δ¹⁸O of ~6.4‰ (Valley, 2003; Bindeman et al., 2004; Bindeman, 2008). δ¹⁸O values above 6.4‰ require the incorporation of sedimentary rocks either by contamination of the mantle source or by assimilation and/or partial melting of a high δ¹⁸O continental crust generated in a low-temperature weathering environment near or at the Earth's surface (e.g., siliciclastic and argillic sediments ~10‰–30‰; Taylor, 1980; Taylor and Sheppard, 1986; Eiler, 2001; Bindeman et al., 2004; Valley et al., 2005; Bindeman, 2008).

The oxygen-isotope values of quartz in the CASP sampled in this study have consistently high δ¹⁸O values, ranging from 8.7‰ to 12.3‰ (Fig. 9). A comparison with published quartz values reveals that the CASP rocks have among the highest measured quartz δ¹⁸O values for silicic volcanic rocks in the world. Similarly high quartz values include ignimbrites within the Great Basin Volcanic Fields, Nevada (>9.0‰–10.9‰; Watts et al., 2016; Watts et al., 2019), Cerro Galan of the Central Andean Ignimbrite Province (9.5‰; Folkes et al., 2013), Glass Mountain, Long Valley, California (9.0‰; Bindeman and Valley, 2002), and the Young Toba Tuff, Indonesia (10.2‰; Budd et al., 2017).

Using the fractionation of 0.6‰ between melt and quartz at 800 °C (Appora et al., 2003; Zhao and Zheng, 2003), the range of magma δ¹⁸O values is 8.1‰–11.7‰. This requires a significant incorporation of materials initially generated near or at the Earth's surface that would cause such high δ¹⁸O values. The mechanisms of making such high SiO₂ bulk wt% magma compositions and high δ¹⁸O melts requires either (1) extensive assimilation of crustal lithologies into mantle-derived melts or (2) pure crustal melting with minimal contribution from the mantle. The established models by which high δ¹⁸O rhyolites are generated typically invoke the mantle as the primary melt and thermal source that incorporates significant crust-derived material via assimilation from 10 up to 50 vol% (e.g., Bindeman and Valley, 2002; Folkes et al., 2013; Bindeman and Simakin, 2014; Budd et al., 2017; González-Maurel et al., 2020; Sas et al., 2022). Within individual eruptive centers, oxygen-isotope variations of more than 2‰ in the crystal record are consistent with heterogeneous proportions of assimilated material. For example, the diverse crystal cargo indicated by quartz values ranging between 6.7‰–10.2‰ in the Young Toba Tuff attests to the long-term assembly of the Toba magmatic system via mantle-derived melts with variations in crustal contributions derived from both high and low δ¹⁸O (e.g., high-temperature, hydrothermally altered) crustal sources (Budd et al., 2017). Purely crustal melts are less commonly invoked as the primary source for rhyolites, largely due to the thermal problems associated with crustal anatexis and high-volume assimilation (e.g., Glazner, 2007; Heinonen et al., 2022). The larger percentages of crustal assimilation (e.g., 50 vol%) require a high heat flux; in these cases, the magmatic episode is often associated with an ignimbrite “flare-up” (e.g., Cerro Galan; Folkes et al., 2013).

For the CASP, the homogeneously high quartz δ¹⁸O values of >9‰ are more consistent with a crustal melting petrogenesis, where widespread crustal

anatexis of a heavy oxygen-enriched felsic crustal source is required to generate the silicic-rich magmas that were erupted partially within an intraplate setting. This is supported by observations of trace-element concentrations that commonly lack chemical differentiation trends consistent with solid-liquid fractionation processes (e.g., Zr/Hf ~30–40; Fig. 5A), and the general absence of abundant mafic to intermediate magmas in the province that would represent parental sources to the voluminous silicic magmas (Fig. 1).

This crustal-like composition in combination with the overall homogeneity of oxygen-isotope values across a large area is particularly impressive when considering the total volume of extruded silicic magma produced (~10,000 km³ for the EQC and 23,000 km³ for the CA; Pankhurst et al., 1998) (Fig. 1A). This scale of widespread homogeneity suggests that the source of these high δ¹⁸O values is unlikely acquired entirely by late-stage assimilation at shallow crustal levels, largely due to the very high thermal fluxes required to melt the upper crust and the large proportions of crust-derived material required to reproduce the δ¹⁸O values measured. Additionally, it is unlikely that mantle-derived magmas would assimilate the same proportion and sample the same crustal assimilation to produce such consistent δ¹⁸O compositions across a vast area (Fig. 1B). Instead, the scale and distribution of such homogeneous compositions indicates that the high δ¹⁸O values were produced by melting a homogeneous high δ¹⁸O source(s) in lower crustal mixing, assimilation, storage, and homogenization (MASH) zones (Hildreth and Moorbath, 1988), where the thermal budget for partial melting of the crust was primarily provided in the form of basaltic underplating following widespread extension (e.g., Bergantz, 1989; Dufek and Bergantz, 2005). Although mass balance models do indicate that open system mixing between crust-derived and mantle-derived melts did occur, we emphasize that the significant mass contribution for the EQC and CA Formation melts was primarily sourced from partial melting of a felsic metasedimentary crust and that the contribution from felsic melts generated via fractionation of mantle-derived magmas was minimal. We use phase petrology constraints to show that this occurred in a thinned continental crust, where the lower crust could be as shallow as 15–18 km (see Constraints on Melting Conditions).

The oxygen-isotope compositions in the CASP are comparable to granites derived by bulk crustal melting of metasedimentary sources (e.g., Blattner et al., 1983; Chappell and White, 1992), including the “S-type” Cape Granites (South Africa; Harris et al., 1997) where calculated melt values of 9.5‰–11.4‰ (quartz values of 11.5‰–13.4‰) correspond to a metasedimentary basement source that has an average δ¹⁸O value of 12.7‰.

Mass Balance Modeling

To understand the contribution of different lithologies to the sources of magma, we use a simple mass balance approach. Here we consider that possible contributions to the δ¹⁸O melt are: (1) mantle-derived melts with a δ¹⁸O value of 5.5‰ (Mattey et al., 1994) and (2) melts from partially melting the

metasedimentary rocks of the underlying continent. We consider the mantle contribution since the mantle upwelling provides the necessary heat required for crustal anatexis (e.g., primarily in the form of basaltic underplating; Riley et al., 2001).

We use the following oxygen-isotope mass balance calculation:

$$\delta^{18}\text{O}_{\text{melt}} = (1-x)\delta^{18}\text{O}_{\text{source}} + x * \delta^{18}\text{O}_{\text{assimilant}} \quad (1)$$

where the x_i 's, where the i is a subscript to the x (as an index), are the molar oxygen ratios of the melts mixed into the erupting melt, and the $\delta^{18}\text{O}_i$ values are the composition of the melt obtained from either partially melting the source (e.g., mantle or crust) or completely assimilating a given rock. Our best estimate for the composition of the La Modesta Formation varies between 8‰–10‰ and 11‰–14‰ for the Bahía de la Lancha based on the variations observed in metamorphic basement rocks outcropping close to the CASP volcanic rocks studied. To simplify the calculations, we choose an end-member value of 12‰ for the Bahía de la Lancha Formation, representing an intermediate $\delta^{18}\text{O}$ value for the metasedimentary samples measured (Table 2). For the La Modesta Formation, we take the uppermost $\delta^{18}\text{O}$ value of 10‰, as lower values would result in assimilation of more than 100% to model the CA Formation melt compositions. Given the uncertainty and variability observed in the metamorphic rocks, we choose to ignore any potential fractionation during (partial) melting of these rocks assuming that the melt obtained corresponds to the bulk-rock isotopic composition. Similarly, we do not include any isotopic fractionations during crystallization. In fact, the $\delta^{18}\text{O}_{\text{melt}}$ is different from $\delta^{18}\text{O}_{\text{magma}}$, since the latter is dependent on the percentage of crystallization of the primary phenocryst phases from the melt (i.e., magma = melt + phenocrysts). However, here our modeled values of melt and magma would be similar due to the low percentage of crystallization in the EQC and CA volcanic rocks (Fig. 3; Table 1).

Target values for the $\delta^{18}\text{O}_{\text{melt}}$ are determined using the equilibrium fractionation factor between quartz and melt ($\Delta^{18}\text{O}_{\text{quartz-rhyolite}}$) of ~0.5‰–0.8‰ for magmatic temperatures of 900 °C to 700 °C, respectively, using the calibrations of Appora et al. (2003) and Zhao and Zheng (2003). We select an intermediate fractionation value of 0.6‰ for a temperature of 800 °C for quartz crystallization, which results in melt compositions that range from 8.7‰ to 11.7‰ for the EQC (average melt = 10.3‰) and from 8.1‰ to 9.8‰ for the CA (average melt = 8.8‰). We tested the effect of changing temperature by performing the same model calculations at both 700 °C and 900 °C. This results in an ~1% change to the mass fraction of assimilated materials and thus has almost no effect on the outcomes of the models.

The sparsity of basement outcrops and the fact that no high-grade metamorphic rocks (e.g., amphibolite or higher grade) were found precludes more detailed models where one could account for changes in local basement along the north-south transect from Lago Posadas versus Los Cóndores. Subtle variations could easily be due to heterogeneities in crustal sources, as discussed later in the Constraints on Melting Conditions section.

The mixing model indicates a minimum of ~55% crustal source and a maximum of 45% of primitive mantle source for all rhyolites and ignimbrites.

This value is obtained by using the lowest quartz values (e.g., 9.5‰ in the EQC and 8.7‰ in the CA) (Fig. 12). However, crustal proportions average 75% for most EQC samples using a basement composition of 12‰. For the CA, with a starting basement composition of 10‰, the magma values in the La Josefina Dome would be 100% crust. For the remaining three CA localities, including the DM rhyolite, Las Lajas ignimbrite, and the Cerro Jorge Paz ignimbrite, a range in mantle proportions of 20%–30% mantle is observed.

These calculations clearly demonstrate, even using average $\delta^{18}\text{O}$ of the EQC and CA, that very high percentages (typically >75%) of crustal material is required. These calculations also demonstrate the differences between the EQC and CA samples. While the mass balance results are similar, the CA melts are nevertheless consistently lower in $\delta^{18}\text{O}$ composition. These lower values correlate with lower $\delta^{18}\text{O}$ values of La Modesta metamorphic rocks (Table 2). This would suggest that the consistently lower $\delta^{18}\text{O}$ values in the CA Formation are best explained by lower $\delta^{18}\text{O}$ values of the crust underlying these volcanic rocks.

Slightly lower proportions of a crustal end member would be required if the starting mantle $\delta^{18}\text{O}$ value was assumed to be an enriched mantle source, where values are considered to range from >6‰ (Eiler, 2001) with values up to 7‰ (Bindeman et al., 2005; Dallai et al., 2019). Mafic and andesitic rocks with enriched $\delta^{18}\text{O}$ compositions have been reported from the Central Andean Volcanic Zone, including Cerro Galan and the Altiplano-Puna Volcanic Complex (Rogers and Hawkesworth, 1989; Kay et al., 2010; Folkes et al., 2013; Freymuth et al., 2015), the Kamchatka Volcanic arc (Bindeman et al., 2004), and from the Famatinian continental arc in Argentina (Cornet et al., 2022).

For the CASP, starting with a high mantle value of 7‰ and considering the same metasedimentary crustal end-member values presented above, the lowest modeled crustal proportions (40%) would correspond to the lowest melt value in the EQC and CA at 8.7‰ and 8.1‰, respectively. However, even with such significant modifications to the mantle source, the average melt $\delta^{18}\text{O}$ value of the EQC and CA still require very high percentages (>70%) of crustal material, determined by the oxygen-isotope values of the metasedimentary basement source(s).

In comparison, less crustal contribution would be required if we would consider a contribution from a highly enriched oxygen-isotope source such as marine carbonates and/or cherts (e.g., >20‰–30‰; Bindeman et al., 2005). While the exposed basement rocks might not be fully representative of the original source rocks in Patagonia, a largely granitic and/or clastic basement source with $\delta^{18}\text{O}$ values roughly between 8‰–16‰ seems likely (e.g., Simon and Lécuyer, 2005). Our chosen values for crustal end members are also consistent with a global xenolith data set for metasedimentary or silicic granulite compositions that report an average $\delta^{18}\text{O}$ value of 10.1‰ (range of 8.5‰–13‰; Kempton and Harmon, 1992).

Constraints on Melting Conditions

The rare occurrence of silicic large igneous provinces throughout the geologic record indicates that a convergence of exceptional circumstances must

be met to generate large volumes of silicic volcanism. The quantity of melt generated during crustal anatexis is determined by the rock composition, the amount of water available for melting, as well as pressure and temperature (e.g., Le Breton and Thompson, 1988; Vielzeuf and Montel, 1994; Gardien et al., 1995; Patiño Douce and Beard, 1995; Patiño Douce, 1999; Bartoli and Carvalho, 2021; Johnson et al., 2021). Fluid produced during prograde metamorphism will typically escape the rocks due to its low density and viscosity, typically as porosity waves (Connolly and Podladchikov, 1998; Connolly and Podladchikov, 2007; Omlin et al., 2018). Hence, the water produced will escape before a rock begins to partially melt. In addition, mobile granitic melts must be undersaturated, generally leading to the proposal of fluid-absent melting of crustal rocks to produce significant amounts of granitic melts (e.g., Thompson, 1982; Clemens, 1984; Stevens and Clemens, 1993; Yardley and Valley, 1997; Patiño Douce, 1999; Clemens et al., 2021). In fluid-absent melting, hydrous minerals (e.g., muscovite, biotite, and hornblende) break down incongruently, supplying volatiles and silicate components to the melt phase (dehydration-melting reactions), leaving behind a refractory assemblage of metamorphic minerals such as aluminosilicates, cordierite, or garnet.

As a likely crustal source, we focus on the volumetrically dominant graywacke compositions in the basement outcrops of both the Bahía de la Lancha and La Modesta Formations (Fig. 2G). Initial partial melting of a graywacke supplies the Si, Ca, Na, and K to produce a silica-rich melt that can range from tonalitic to granitic in composition, depending on the P - T conditions (e.g., Montel and Vielzeuf, 1997; Patiño Douce, 1999). While volumetrically less abundant, the interbedded pelitic layers are significant as they could provide a source of water, which promotes melting of the graywacke at lower temperatures (e.g., Thompson and Connolly, 1995).

With these constraints in mind, we modeled the partial melting of the potential source rock compositions, allowing fluid to escape until first melting occurred. Subsequently, we model the fluid-absent melting (referring here only to a H_2O -dominated phase) of the basement graywacke compositions (Table 2) using the thermodynamic equilibrium programs of THERIAK-DOMINO (de Capitani and Petrakakis, 2010) with the data set *tcds55_p07n* (converted to THERIAK-DOMINO format by D.K. Tinkham; <https://dtinkham.net/peq.html>). A summary of the input bulk-rock composition and the references to the solution models used is provided in File S6 (footnote 1). We set our model temperatures based on the analysis of Huppert and Sparks (1988), which predicts felsic magmas generated via crustal anatexis would have a peak temperature of ~ 900 °C at 5 kbar (fluid-absent melting), following the intrusion of mafic magma.

Partition coefficients determined for the heavy REE between garnet and a felsic melt are one order of magnitude greater than that for other (commonly) observed mineral phases in a graywacke (e.g., Arth, 1976). Garnet modal abundances greater than five percent will result in a melt with a depleted heavy REE signature, typical for a garnet-bearing source. The low La/Yb ratios and large Eu anomalies of the EQC and CA volcanic rocks and general absence of a strong garnet signature in the REE patterns requires that the modal abundance of

garnet equilibrated with the melt is small (Fig. 6) and instead indicate a source region dominated by a low-pressure mineralogy (e.g., feldspar, micas, and pyroxene; Kay et al., 1991). An exception are the volcanic rocks from the La Josefina Dome. Unsurprisingly, Figure 13 reveals that garnet becomes more and more stable at high pressures. Small amounts of garnet are typically observed at pressures less than 5 kbar, which corresponds to a depth of melting of less than 15–18 km, depending on the average density of the crust. Thus, these low pressures are either associated with a thin crust, or alternatively, melting is required in the middle crust for an average crust thickness of 30 km.

The thermodynamic modeling reveals that subtle variations in bulk-rock compositions lead to major changes in equilibrium assemblages and modal abundances at a given pressure. Melt volumes produced within the crust at 900 °C during fluid-absent melting of some graywacke compositions resulted in liquid volumes of $\sim 55\%$ – 60% (Figs. 14 and 15). The bulk-rock composition of LPMF12 produced the largest liquid volume (60%) with an equilibrated phase assemblage of albite, K-feldspar, quartz, biotite, sillimanite, cordierite, garnet, and muscovite (Fig. 15B), in comparison to LPMF11 in which only one feldspar was stable at a given temperature (Fig. 15A). In both cases, the earliest onset of melting at 650 °C began due to the presence of muscovite at the solidus. These modeling results and liquid volume calculations are consistent with the graywacke partial melting experimental studies of Vielzeuf and Montel (1994). Similar to decompression melting, larger volumes of melt are produced at lower pressure for a given temperature (e.g., 900 °C). Water solubility in melts increases with pressure (e.g., Holtz et al., 2001), and hence, for a given amount of water originally contained in the hydrous minerals, a larger proportion of melting will be observed in a thinned crust at pressures of 5 kbar than would be produced at pressures of 10 kbar, which are typical for crustal thicknesses of ~ 35 km.

The models indicate that the absence of muscovite at the solidus in the slightly more mafic and calcic La Modesta graywacke (LMJMF5) produces a prolonged melting reaction, following the slow break-down of biotite from the onset of melting (first liquid) at ~ 680 until 840 °C (Fig. 15C). Due to the lack of abundant hydrous phases in LMJMF5, a liquid volume of only 30% was reached at 900 °C. In both the LPMF13 and EEMF14 graywacke compositions, similar compositions with high silica contents of >80 wt% bulk SiO_2 resulted in the lowest melt volume produced (e.g., $<20\%$) due to the abundance of refractory phases (Figs. 14 and 15D). Similarly, partial melting of pelites also produces less granitic melt, since the absence of sodium-rich phases restricts melting (e.g., Patiño Douce, 1999).

These results indicate that the basement lithologies associated with the EQC and the CA regions can produce significant melt volumes at temperatures even less than 900 °C at moderate pressures and have correspondingly high $\delta^{18}O$ values (Table 2). Bulk-rock compositions that have equilibrated muscovite at the onset of melting are the most likely candidates for the generation of large volumes of melt. In addition, our modeling results show the dependence of melt volumes generated during anatexis on the starting modal proportions of quartz and feldspar (Fig. 15).

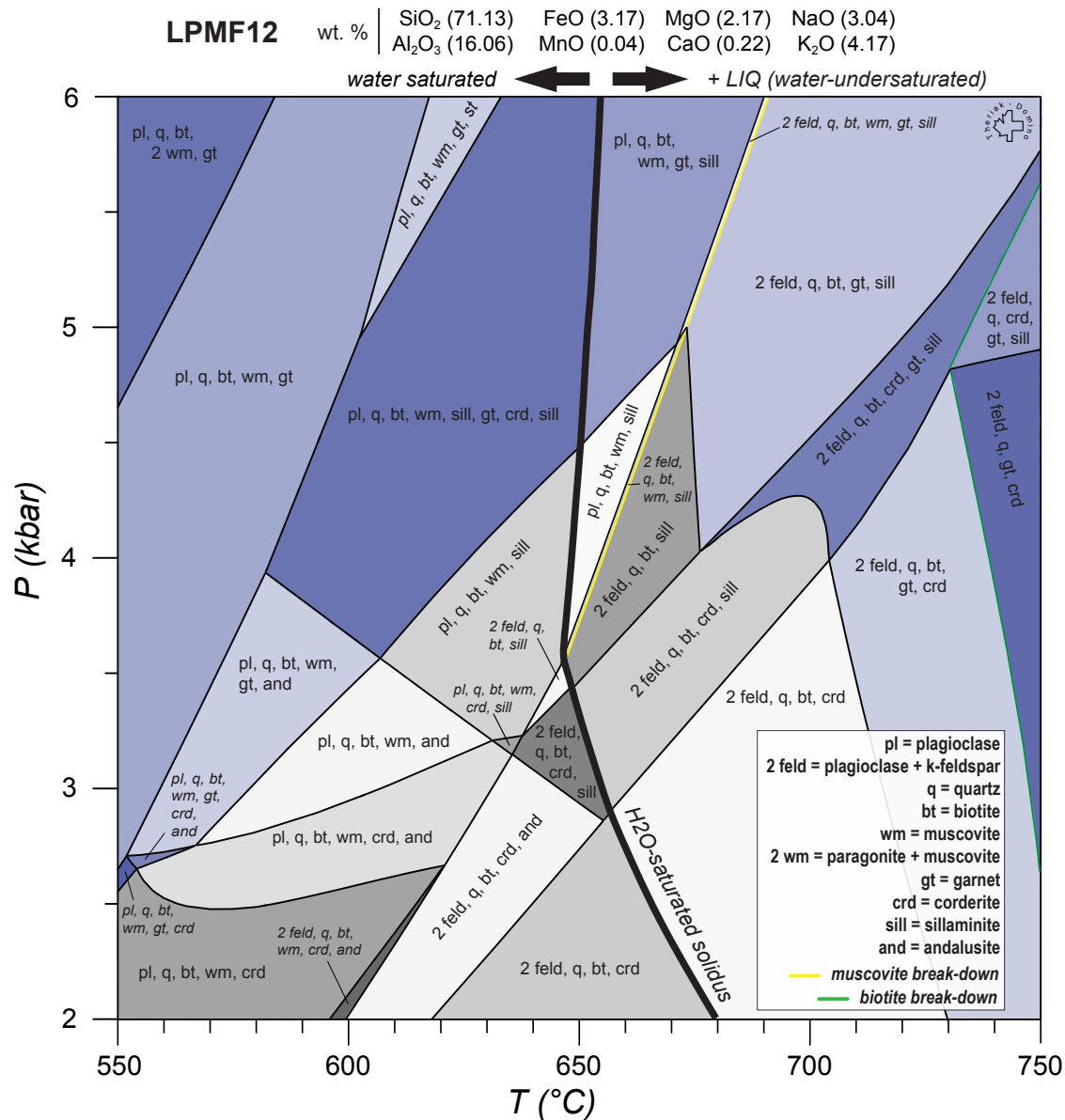


Figure 13. Metamorphic phase diagram of a Bahía de la Lancha graywacke sample (LPMF12). Below the solidus, the equilibrium phase assemblage is calculated at water-saturated conditions. Above the solidus, the phase assemblages are calculated using the water concentration determined for 5 kbar such that the water present is bound in hydrous phases. The stability field of garnet is indicated in blue and increases with increasing pressure. Although garnet is stable at 5 kbar, the modal abundance of garnet is less than 5% by volume at this pressure. Models are calculated using the thermodynamic equilibrium programs of THERIAK-DOMINO (de Capitani and Petrakakis, 2010), using the data set *tcds55_p07n*.

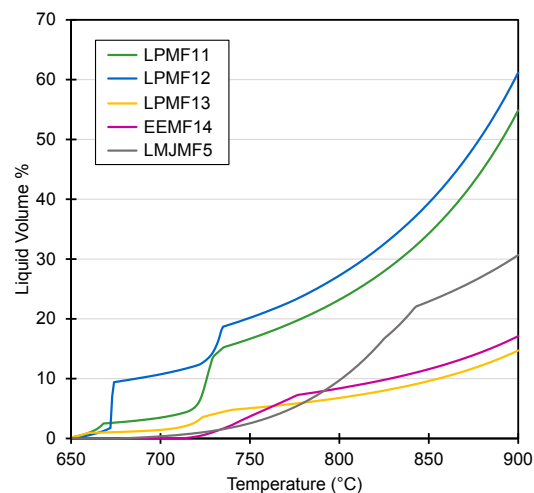


Figure 14. Liquid volume calculations for fluid-absent melting of graywacke compositions in the Bahía de la Lancha and La Modesta Formation at 5 kbar from 650 to 900 °C.

Note that our results cannot account for local changes in bulk $X\text{-H}_2\text{O}$ composition that could result after the loss of the first melt production, due to upward migration. Initial melt compositions produced from partial melting of a graywacke will be close to the granite minimum composition (Montel and Vielzeuf, 1997; Patiño Douce, 1999); subsequent extraction of this melt will leave a residual refractory rock that becomes harder to melt at lower temperatures, thus leading to lower melt volume fractions produced at the same temperature. Oppositely, the influx of water-rich melts or water from pelite dehydration would further promote melting at the same temperature.

CONCLUSIONS

We obtained a large oxygen-isotope data set on quartz phenocryst using SIMS ($n = 536$) and LF methods. Our data show that the silicic volcanic rocks of El Quemado Complex and Chon Aike Formation are characterized by high oxygen-isotope values between 9.1‰–12.3‰, which are some of the highest $\delta^{18}\text{O}$ values measured in a silicic large igneous province and for rhyolites worldwide. We demonstrate that the oxygen-isotope data for quartz phenocryst reliably record magma $\delta^{18}\text{O}$ compositions, while the matrix is significantly altered by hydrothermal alteration. Single spot $\delta^{18}\text{O}$ analyses of individual quartz grains display homogeneous compositions despite complex CL zoning; these compositions reflect complicated growth histories, including some dissolution-regrowth events. Oxygen isotopes can re-equilibrate

via diffusion in ~100 k.y. at 800 °C, and even faster at 900 °C, so that oxygen-isotope compositions of quartz record the magmatic melt composition shortly before eruption.

Oxygen-isotope mass balance calculations demonstrate that the EQC and CA contain a large proportion of crust-derived melts (on average, >75%). Although, even with these high percentages of crust-derived melts, some mantle melt components were likely added. The large volumes of high $\delta^{18}\text{O}$ magmas, as well as their occurrence over a large domain requires favorable crustal melt conditions. The absence of a typical garnet signature in the rhyolite REE trace-element pattern suggests that the role of garnet in the crustal source is negligible. Based on thermodynamic modeling, this points to a shallow depth (~15 km) for the focus of crustal melting. The most probable source rocks in southern Patagonia are predominately of graywacke composition, similar to the Bahía de la Lancha and La Modesta formations. This might help to explain numerous geochemical and isotopic observations, including the widespread high $\delta^{18}\text{O}$ composition, the inherited “VAG” bulk-rock composition, the negative Eu-anomaly composition indicating abundant feldspar (plagioclase) in the residual cumulate source, and the characteristically high Zr/Hf ratios in the bulk rock of the volcanic units.

The fertile rock compositions dominated by graywacke and pelitic rock types deposited along the active paleo-Pacific margin of southern Patagonia during the Paleozoic (e.g., Hervé, 1988; Ramos, 2008; Permuy-Vidal et al., 2014; Suárez et al., 2019) provide the ideal source for readily fusible material for the magmas of the EQC and CA. To reach the high temperatures recorded in the rhyolite magmas of at least 900 °C (e.g., Seitz et al., 2018b), large amounts of heat must be advected to this part of the crust. A tectonic scenario in which the crust-mantle boundary is shallow, and hence significant amounts of heat can be advected to the base of the thin crust, favors melting at low pressures (<5 kbar), which in turn allows for significant amounts of melt to be produced by fluid-absent melting that triggered widespread volcanic activity in southern Patagonia. For significant melting to occur during the CASP magmatic flare-up events, the crust should not have been metamorphosed at temperatures exceeding the partial melting (e.g., 650 °C), as remelting of partially molten precursors (i.e., residual refractory rocks) is much less favorable for obtaining large volumes of melts.

Although tectonic drivers and thermal considerations are under discussion for the Chon Aike Silicic Large Igneous Province (e.g., Pankhurst et al., 2000; Riley et al., 2001; Navarrete et al., 2019; Bastias et al., 2021), with further work in progress (Foley et al., 2021, 2022b), we conclude that the occurrence of the Chon Aike Silicic Large Igneous Province was likely favored by an orogenic cycle in which low- to middle-grade metamorphic rocks of sedimentary origin are positioned close to the mantle in a thinned, extended crust and were then intruded by mafic melts extracted from the mantle. Widespread extension and subsequent lithospheric thinning leading to the injection and emplacement of basaltic magmas into the lower crust (e.g., Riley et al., 2001) provides the necessary thermal environment for the partial melting of the crustal rocks at mid-crustal levels.

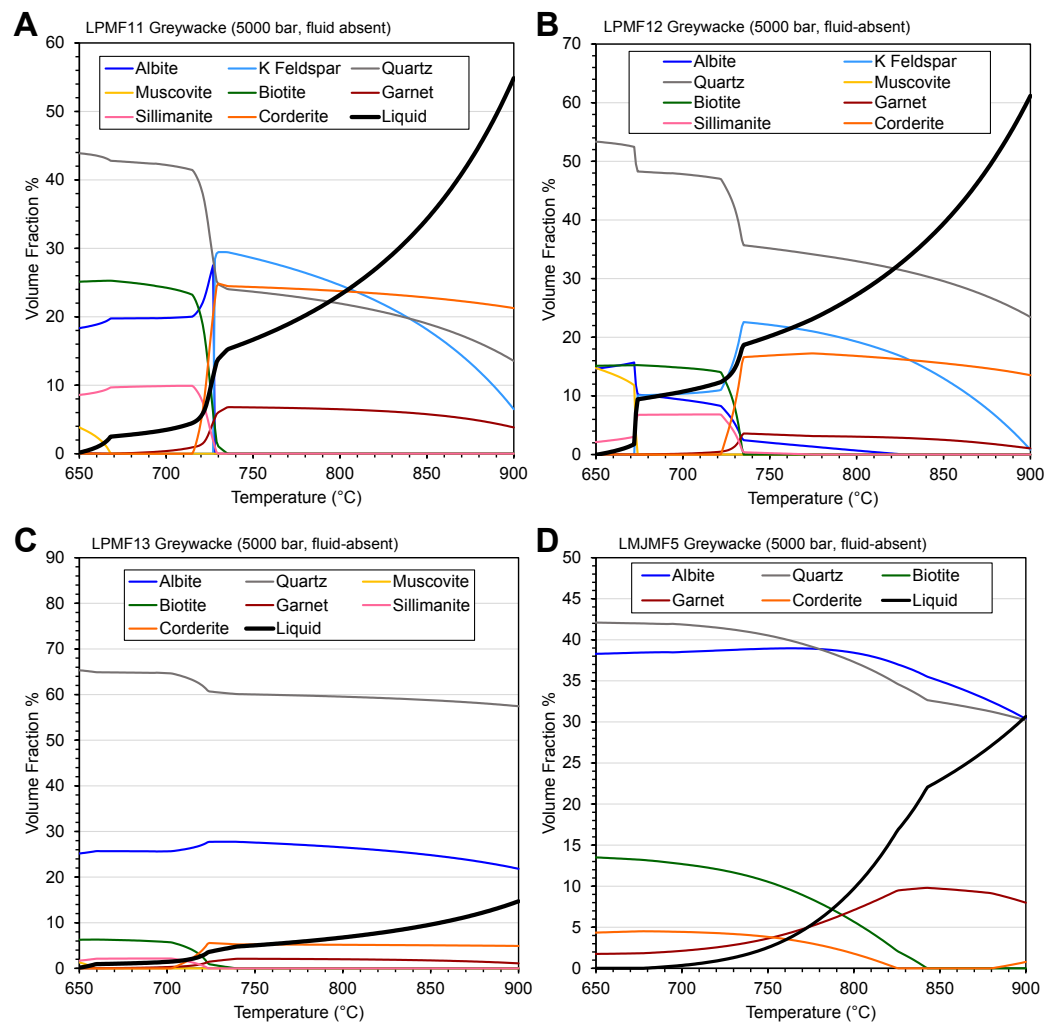


Figure 15. Fluid-absent melting reactions from 650 to 900 °C of different graywacke compositions from the (A–C) Bahía de la Lancha and (D) La Modesta Formation. (A and B) The largest melt (liquid) volume fractions are generated in the graywacke compositions with muscovite stable at the solidus. (C) Graywacke composition with large volumes of initial quartz resulted in the lowest melt volume produced. See Figure 13 caption for reference to the model’s data set.

ACKNOWLEDGMENTS

This themed issue is dedicated to the career of Calvin Miller and highlights his lifelong, passionate inquisitiveness and dedication to understanding issues relating to the source, transport, and storage of silicic magmas. We are grateful for his contributions, which allowed this work to build upon the ideas he crafted. We thank the authorities of the Parque Nacional de los Glaciares (Argentina) for their support and permission to sample in the region of El Chaltén. We also thank Vicente Sánchez, the Head Geologist, and the staff of the La Josefina Project (Hunt Mining) for their generosity and openness to sharing geological knowledge and resources on site. The major and trace-element bulk-rock analyses were conducted with the assistance of Olivier Reubi (XRF; University of Lusanne [UNIL]) and Alexey Ulyanov (LA-ICP-MS; UNIL). We are also grateful to Torsten Vennemann for granting access to the Stable Isotope Laboratory of UNIL. This research was funded by the Swiss National Science Foundation (200021_175808 to BP). The WiscSIMS

instrumentation was partially supported by National Science Foundation (EAR-1658823). The final versions of this manuscript benefited from additional edits and thoughtful contributions from D.O. Zakharov and R.J. Pankhurst. We also express our thanks for the thoughtful reviews from Anita Grunder and Teal Riley with their suggestions and comments, which improved the original manuscript. Lastly, we thank Jonathan Miller and Shanaka de Silva for their editorial handling.

REFERENCES CITED

Alperin, M., Echeveste, H., Fernández, R., and Bellieni, G., 2007, Análisis estadístico de datos geoquímicos de volcanitas jurásicas del Macizo del Deseado, Provincia de Santa Cruz: Revista de la Asociación Geológica Argentina, v. 62, p. 200–209.

- Appora, I., Eiler, J.M., Matthews, A., and Stolper, E.M., 2003, Experimental determination of oxygen isotope fractionations between CO₂ vapor and soda-melilitite melt: *Geochimica et Cosmochimica Acta*, v. 67, no. 3, p. 459–471, [https://doi.org/10.1016/S0016-7037\(02\)01090-6](https://doi.org/10.1016/S0016-7037(02)01090-6).
- Arth, J.G., 1976, Behavior of trace elements during magmatic processes: A summary of theoretical models and their applications: *Journal of Research of the U.S. Geological Survey*, v. 4, p. 41–47.
- Augustsson, C., Münker, C., Bahlburg, H., and Fanning, M., 2006, Provenance of late Palaeozoic metasediments of the SW South American Gondwana margin: A combined U-Pb and Hf-isotope study of single detrital zircons: *Journal of the Geological Society*, v. 163, no. 6, p. 983–995, <https://doi.org/10.1144/0016-76492005-149>.
- Baker, P.E., Rea, W.J., Skarmeta, J., Caminos, R., and Rex, D.C., 1981, Igneous history of the Andean Cordillera and Patagonian Plateau around Latitude 46°S: *Philosophical Transactions of the Royal Society of London. Series B, Biological Sciences*, v. 303, p. 105–149, <https://doi.org/10.1098/rsta.1981.0194>.
- Bartoli, O., and Carvalho, B.B., 2021, Anatectic granites in their source region: A comparison between experiments, thermodynamic modeling and nanogranitoids: *Lithos*, v. 402–403, <https://doi.org/10.1016/j.lithos.2021.106046>.
- Bastias, J., Spikings, R., Riley, T., Ulyanov, A., Grunow, A., Chiaradia, M., and Hervé, F., 2021, A revised interpretation of the Chon Aike magmatic province: Active margin origin and implications for the opening of the Weddell Sea: *Lithos*, v. 386–387, <https://doi.org/10.1016/j.lithos.2021.106013>.
- Bergantz, G.W., 1989, Underplating and partial melting: Implications for melt generation and extraction: *Science*, v. 245, no. 4992, p. 1093–1095, <https://doi.org/10.1126/science.245.4922.1093>.
- Bindeman, I.N., 2008, Oxygen isotopes in mantle and crustal magmas as revealed by single crystal analysis: *Reviews in Mineralogy and Geochemistry*, v. 69, no. 1, p. 445–478, <https://doi.org/10.2138/rmg.2008.69.12>.
- Bindeman, I.N., and Simakin, A.G., 2014, Rhyolites—Hard to produce, but easy to recycle and sequester: Integrating microgeochemical observations and numerical models: *Geosphere*, v. 10, no. 5, p. 930–957, <https://doi.org/10.1130/GES00969.1>.
- Bindeman, I.N., and Valley, J.W., 2002, Oxygen isotope study of the Long Valley magma system, California: Isotope thermometry and convection in large silicic magma bodies: *Contributions to Mineralogy and Petrology*, v. 144, p. 185–205, <https://doi.org/10.1007/s00410-002-0371-8>.
- Bindeman, I.N., Ponomareva, V.V., Bailey, J.C., and Valley, J.W., 2004, Volcanic arc of Kamchatka: A province with high- $\delta^{18}\text{O}$ magma sources and large-scale $^{18}\text{O}/^{16}\text{O}$ depletion of the upper crust: *Geochimica et Cosmochimica Acta*, v. 68, no. 4, p. 841–865, <https://doi.org/10.1016/j.gca.2003.07.009>.
- Bindeman, I.N., Eiler, J.M., Yogodzinski, G.M., Tatsumi, Y., Stern, C.R., Grove, T.L., Portnyagin, M., Hoernle, K., and Danyushevsky, L.V., 2005, Oxygen isotope evidence for slab melting in modern and ancient subduction zones: *Earth and Planetary Science Letters*, v. 235, no. 3–4, p. 480–496, <https://doi.org/10.1016/j.epsl.2005.04.014>.
- Blattner, P., Dietrich, V., and Gansser, A., 1983, Contrasting ^{18}O enrichment and origins of High Himalayan and Transhimalayan intrusives: *Earth and Planetary Science Letters*, v. 65, no. 2, p. 276–286, [https://doi.org/10.1016/0012-821X\(83\)90166-8](https://doi.org/10.1016/0012-821X(83)90166-8).
- Bouhier, V.E., Franchini, M.B., Caffè, P.J., Maydagán, L., Rapela, C.W., and Paolini, M., 2017, Petrogenesis of volcanic rocks that host the world-class Ag-Pb Navidad District, North Patagonian Massif: Comparison with the Jurassic Chon Aike Volcanic Province of Patagonia, Argentina: *Journal of Volcanology and Geothermal Research*, v. 338, p. 101–120, <https://doi.org/10.1016/j.jvolgeores.2017.03.016>.
- Bucholz, C.E., Jagoutz, O., VanTongeren, J.A., Setera, J., and Wang, Z., 2017, Oxygen isotope trajectories of crystallizing melts: Insights from modeling and the plutonic record: *Geochimica et Cosmochimica Acta*, v. 207, p. 154–184, <https://doi.org/10.1016/j.gca.2017.03.027>.
- Budd, D.A., Troll, V.R., Deegan, F.M., Jolis, E.M., Smith, V.C., Whitehouse, M.J., Harris, C., Freda, C., Hilton, D.R., Halldórsson, S.A., and Bindeman, I.N., 2017, Magma reservoir dynamics at Toba caldera, Indonesia, recorded by oxygen isotope zoning in quartz: *Scientific Reports*, v. 7, <https://doi.org/10.1038/srep40624>.
- Chappell, B.W., and White, A.J.R., 1992, I- and S-type granites in the Lachlan Fold Belt: *Earth and Environmental Science Transactions of the Royal Society of Edinburgh: Earth Sciences*, v. 83, no. 1–2, p. 1–26, <https://doi.org/10.1017/S0263593300007720>.
- Cherniak, D.J., Watson, E.B., and Wark, D.A., 2007, Ti diffusion in quartz: *Chemical Geology*, v. 236, no. 1–2, p. 65–74, <https://doi.org/10.1016/j.chemgeo.2006.09.001>.
- Clemens, J.D., 1984, Water contents of intermediate to silicic magmas: *Lithos*, v. 17, p. 273–287, [https://doi.org/10.1016/0024-4937\(84\)90025-2](https://doi.org/10.1016/0024-4937(84)90025-2).
- Clemens, J.D., Stevens, G., and Bryan, S.E., 2020, Conditions during the formation of granitic magmas by crustal melting—Hot or cold; drenched, damp, or dry?: *Earth-Science Reviews*, v. 200, <https://doi.org/10.1016/j.earscirev.2019.102982>.
- Clemens, J.D., Stevens, G., and Mayne, M.J., 2021, Do arc silicic magmas form by fluid-fluxed melting of older arc crust or fractionation of basaltic magmas?: *Contributions to Mineralogy and Petrology*, v. 176, article no. 44, <https://doi.org/10.1007/s00410-021-01800-w>.
- Connolly, J.A.D., and Podladchikov, Y.Y., 1998, Compaction-driven fluid flow in viscoelastic rock: *Geodinamica Acta*, v. 11, no. 2–3, p. 55–84, <https://doi.org/10.1080/09853111.1998.11105311>.
- Connolly, J.A.D., and Podladchikov, Y.Y., 2007, Decompaction weakening and channeling instability in ductile porous media: Implications for asthenospheric melt segregation: *Journal of Geophysical Research: Solid Earth*, v. 112, no. B10, <https://doi.org/10.1029/2005JB004213>.
- Cornet, J., Laurent, O., Wotzlav, J.-F., Antonelli, M.A., Otamendi, J., Bergantz, G., and Bachmann, O., 2022, Reworking subducted sediments in arc magmas and the isotopic diversity of the continental crust: The case of the Ordovician Famatinian crustal section, Argentina: *Earth and Planetary Science Letters*, v. 595, <https://doi.org/10.1016/j.epsl.2022.117706>.
- Dallai, L., Bianchini, G., Avanzinelli, R., Natali, C., and Conticelli, S., 2019, Heavy oxygen recycled into the lithospheric mantle: *Scientific Reports*, v. 9, article no. 8793, <https://doi.org/10.1038/s41598-019-45031-3>.
- de Capitani, C., and Petrakakis, K., 2010, The computation of equilibrium assemblage diagrams with Theriak/Domino software: *American Mineralogist*, v. 95, no. 7, p. 1006–1016, <https://doi.org/10.2138/am.2010.3354>.
- DePaolo, D.J., 1981, A neodymium and strontium isotopic study of the Mesozoic calc-alkaline granitic batholiths of the Sierra Nevada and Peninsular Ranges, California: *Journal of Geophysical Research: Solid Earth*, v. 86, no. B11, p. 10,470–10,488, <https://doi.org/10.1029/JB086B11p10470>.
- DePaolo, D.J., Perry, F.V., and Baldrige, W.S., 1992, Crustal versus mantle sources of granitic magmas: A two-parameter model based on Nd isotopic studies: *Earth and Environmental Science Transactions of the Royal Society of Edinburgh*, v. 83, no. 1–2, p. 439–446, <https://doi.org/10.1017/S0263593300008117>.
- Dufek, J., and Bergantz, G.W., 2005, Lower crustal magma genesis and preservation: A stochastic framework for the Evaluation of basalt-crust interaction: *Journal of Petrology*, v. 46, no. 11, p. 2167–2195, <https://doi.org/10.1093/petrology/egi049>.
- Echeveste, H., and Fernández, R., 2012, Fragmentación por Flujo en la Ignimbrita Las Lajas, Formación Chon Aike, Macizo Del Deseado: *Revista de la Asociación Geológica Argentina*, v. 69, p. 61–71.
- Echeveste, H., Páez, G., López, L., Carlini, M., and De Martino, F., 2020, El Complejo Volcánico Bahía Laura en la zona del distrito minero Manantial Espejo: *Revista del Museo de La Plata*, v. 5, no. 1, p. 1–35, <https://doi.org/10.24215/25456377e092>.
- Eiler, J.M., 2001, Oxygen isotope variations of basaltic lavas and upper mantle rocks: *Reviews in Mineralogy and Geochemistry*, v. 43, no. 1, p. 319–364, <https://doi.org/10.2138/gsrmg.43.1.319>.
- Feeley, T.C., Clyne, M.A., Winer, G.S., and Grice, W.C., 2008, Oxygen isotope geochemistry of the Lassen Volcanic Center, California: Resolving crustal and mantle contributions to continental arc magmatism: *Journal of Petrology*, v. 49, no. 5, p. 971–997, <https://doi.org/10.1093/petrology/egn013>.
- Féraud, G., Alric, V., Fornari, M., Bertrand, H., and Haller, M., 1999, $^{40}\text{Ar}/^{39}\text{Ar}$ dating of the Jurassic volcanic province of Patagonia: Migrating magmatism related to Gondwana break-up and subduction: *Earth and Planetary Science Letters*, v. 172, no. 1–2, p. 83–96, [https://doi.org/10.1016/S0012-821X\(99\)00190-9](https://doi.org/10.1016/S0012-821X(99)00190-9).
- Foley, M.L., Putlitz, B., Baumgartner, L.P., Ulyanov, A., and Siron, G., 2021, Isotope characteristics of a large silicic province: Crustal versus mantle processes in the generation of the Jurassic Chon Aike Silicic Province (Argentina): *Geological Society of America Abstracts with Programs*, v. 53, no. 6, <https://doi.org/10.1130/abs/2021AM-367996>.
- Foley, M.L., Guillermin, Z., Putlitz, B., and Baumgartner, L.P., 2022a, Zircon U-Pb ages in El Chaltén Jurassic rhyolites (Chon Aike Silicic LIP, Argentina) reveal xenocrystic remnants of an unexposed lower basement of the paleo-Pacific Gondwana margin: *Journal of South American Earth Sciences*, v. 114, <https://doi.org/10.1016/j.jsames.2021.103690>.
- Foley, M.L., Gaynor, S.P., Putlitz, B., and Baumgartner, L.P., 2022b, High-Precision Geochronology in the El Quemado Complex of the Chon Aike Silicic Large Igneous Province: A Short High-Flux Event within a Longer-Lived SLIP: Santiago, Chile, XII South American Symposium on Isotope Geology, 3–6 July.
- Folkes, C.B., de Silva, S.L., Bindeman, I.N., and Cas, R.A.F., 2013, Tectonic and climate history influence the geochemistry of large-volume silicic magmas: New $\delta^{18}\text{O}$ data from the Central

- Andes with comparison to N America and Kamchatka: *Journal of Volcanology and Geothermal Research*, v. 262, p. 90–103, <https://doi.org/10.1016/j.jvolgeores.2013.05.014>.
- Freytmuth, H., Brandmeier, M., and Wörner, G., 2015, The origin and crust/mantle mass balance of Central Andean ignimbrite magmatism constrained by oxygen and strontium isotopes and erupted volumes: *Contributions to Mineralogy and Petrology*, v. 169, article no. 58, <https://doi.org/10.1007/s00410-015-1152-5>.
- Gardien, V., Thompson, A.B., Grujic, D., and Ulmer, P., 1995, Experimental melting of biotite + plagioclase + quartz ± muscovite assemblages and implications for crustal melting: *Journal of Geophysical Research: Solid Earth*, v. 100, no. B8, p. 15,581–15,591, <https://doi.org/10.1029/95JB00916>.
- Giacosa, R., Fracchia, D., and Heredia, N., 2012, Structure of the Southern Patagonian Andes at 49°S, Argentina: *Geologica Acta*, v. 10, no. 3, p. 265–282, <https://doi.org/10.1344/105.000001749>.
- Glazner, A.F., 2007, Thermal limitations on incorporation of wall rock into magma: *Geology*, v. 35, no. 4, p. 319–322, <https://doi.org/10.1130/G23134A.1>.
- González-Maurel, O., Deegan, F.M., le Rouz, P., Harris, C., Troll, V.R., and Godoy, B., 2020, Constraining the sub-arc, parental magma composition for the giant Altiplano-Puna Volcanic Complex, northern Chile: *Scientific Reports*, v. 10, article no. 6864, <https://doi.org/10.1038/s41598-020-63454-1>.
- Gualda, G.A.R., and Sutton, S.R., 2016, The Year Leading to a Supereruption: *PLOS ONE*, v. 11, no. 7, <https://doi.org/10.1371/journal.pone.0159200>.
- Guido, D., Escayola, M., de Barrio, R., Schalamuk, I., and Franz, G., 2006, La Formación Bajo Pobre (Jurásico) en el este del Macizo del Deseado, Patagonia: Vinculación con el Grupo Bahía Laura: *Revista de la Asociación Geológica Argentina*, v. 61, p. 187–196.
- Gust, D.A., Biddle, K.T., Phelps, D.W., and Uliana, M.A., 1985, Associated Middle to Late Jurassic volcanism and extension in southern South America: *Tectonophysics*, v. 116, no. 3–4, p. 223–253, [https://doi.org/10.1016/0040-1951\(85\)90210-0](https://doi.org/10.1016/0040-1951(85)90210-0).
- Harris, C., Faure, K., Diamond, R.E., and Scheepers, R., 1997, Oxygen and hydrogen isotope geochemistry of S- and I-type granitoids: The Cape Granite suite, South Africa: *Chemical Geology*, v. 143, no. 1–2, p. 95–114, [https://doi.org/10.1016/S0009-2541\(97\)00103-4](https://doi.org/10.1016/S0009-2541(97)00103-4).
- Heinonen, J.S., Spera, F.J., and Bohrsen, W.A., 2022, Thermodynamic limits for assimilation of silicate crust in primitive magmas: *Geology*, v. 50, no. 1, p. 81–85, <https://doi.org/10.1130/G49139.1>.
- Hervé, F., 1988, Late Paleozoic subduction and accretion in southern Chile: Episodes, *Journal of International Geoscience*, v. 11, no. 3, p. 183–188, <https://doi.org/10.18814/epiugs/1988/v11i3/005>.
- Hervé, F., Fanning, C.M., and Pankhurst, R.J., 2003, Detrital zircon age patterns and provenance in the metamorphic complexes of southern Chile: *Journal of South American Earth Sciences*, v. 16, no. 1, p. 107–123, [https://doi.org/10.1016/S0895-9811\(03\)00022-1](https://doi.org/10.1016/S0895-9811(03)00022-1).
- Hervé, F., Pankhurst, R.J., Fanning, C.M., Calderón, M., and Yaxley, G.M., 2007, The South Patagonian batholith: 150 my of granite magmatism on a plate margin: *Lithos*, v. 97, no. 3–4, p. 373–394, <https://doi.org/10.1016/j.lithos.2007.01.007>.
- Hervé Allamand, F., Calderón, M., and Faúndez, V., 2008, The metamorphic complexes of the Patagonian and Fuegian Andes: *Geologica Acta*, v. 6, no. 1, p. 43–53, <https://doi.org/10.1344/105.000000240>.
- Hildreth, W., and Moorbath, S., 1988, Crustal contributions to arc magmatism in the Andes of Central Chile: *Contributions to Mineralogy and Petrology*, v. 98, p. 455–489, <https://doi.org/10.1007/BF00372365>.
- Hildreth, W., Halliday, A.N., and Christiansen, R.L., 1991, Isotopic and chemical evidence concerning the genesis and contamination of basaltic and rhyolitic magma beneath the Yellowstone Plateau Volcanic Field: *Journal of Petrology*, v. 32, no. 1, p. 63–138, <https://doi.org/10.1093/petrology/32.1.63>.
- Holtz, F., Johannes, W., Tamic, N., and Behrens, H., 2001, Maximum and minimum water contents of granitic melts generated in the crust: A reevaluation and implications: *Lithos*, v. 56, no. 1, p. 1–14, [https://doi.org/10.1016/S0024-4937\(00\)00056-6](https://doi.org/10.1016/S0024-4937(00)00056-6).
- Huppert, H.E., and Sparks, S.J., 1988, The generation of granitic magmas by intrusion of basalt into continental crust: *Journal of Petrology*, v. 29, no. 3, p. 599–624, <https://doi.org/10.1093/petrology/29.3.599>.
- Jackson, S.E., 2008, LAMTRACE data reduction software for LA-ICP-MS, in *Sylvester, P. ed., Laser Ablation ICP-MS in the Earth Sciences: Current Practices and Outstanding Issues: Short Course Series*, Mineralogical Association of Canada, v. 40, p. 305–307, https://www.researchgate.net/publication/254544236_LAMTRACE_data_reduction_software.
- Jacob, J.-B., Moyen, J.-F., Fiannacca, P., Laurent, O., Bachmann, O., Janoušek, V., Farina, F., and Villaros, A., 2021, Crustal melting vs. fractionation of basaltic magmas: Part 2, Attempting to quantify mantle and crustal contributions in granitoids: *Lithos*, v. 402–403, <https://doi.org/10.1016/j.lithos.2021.106292>.
- Johnson, T., Yakymchuk, C., and Brown, M., 2021, Crustal melting and supresolidus phase equilibria: From first principles to the state-of-the-art: *Earth-Science Reviews*, v. 221, <https://doi.org/10.1016/j.earscirev.2021.103778>.
- Jollands, M.C., Bloch, B., and Müntener, O., 2020, New Ti-in-quartz diffusivities reconcile natural Ti zoning with time scales and temperatures of upper crustal magma chamber reservoirs: *Geology*, v. 48, no. 7, p. 654–657, <https://doi.org/10.1130/G47238.1>.
- Kay, S.M., Ramos, V.A., Mpodozis, C., and Sruoga, P., 1989, Late Paleozoic to Jurassic silicic magmatism at the Gondwana margin: Analogy to the Middle Proterozoic in North America? *Geology*, v. 17, no. 4, p. 324–328, [https://doi.org/10.1130/0091-7613\(1989\)017<0324:LPTJSM>2.3.CO;2](https://doi.org/10.1130/0091-7613(1989)017<0324:LPTJSM>2.3.CO;2).
- Kay, S.M., Mpodozis, C., Ramos, V.A., and Munizaga, F., 1991, Magma source variations for mid-late Tertiary magmatic rocks associated with a shallowing subduction zone and thickening crust in the central Andes (28 to 33 °S), in *Harmon, R.S. and Rapela, C.W., eds., Andean Magmatism and Its Tectonic Setting: Geological Society of America Special Paper 265*, p. 113–138, <https://doi.org/10.1130/SPE265-p113>.
- Kay, S.M., Coira, B.L., Caffè, P.J., and Chen, C.-H., 2010, Regional chemical diversity, crustal and mantle sources and evolution of central Andean Puna plateau ignimbrites: *Journal of Volcanology and Geothermal Research*, v. 198, no. 1–2, p. 81–111, <https://doi.org/10.1016/j.jvolgeores.2010.08.013>.
- Kempton, P.D., and Harmon, R.S., 1992, Oxygen isotope evidence for large-scale hybridization of the lower crust during magmatic underplating: *Geochimica et Cosmochimica Acta*, v. 56, no. 3, p. 971–986, [https://doi.org/10.1016/0016-7037\(92\)90041-G](https://doi.org/10.1016/0016-7037(92)90041-G).
- Kita, N.T., Ushikubo, T., Fu, B., and Valley, J.W., 2009, High precision SIMS oxygen isotope analysis and the effect of sample topography: *Chemical Geology*, v. 264, no. 1–4, p. 43–57, <https://doi.org/10.1016/j.chemgeo.2009.02.012>.
- Lacroix, B., and Vennemann, T., 2015, Empirical calibration of the oxygen isotope fractionation between quartz and Fe-Mg-chlorite: *Geochimica et Cosmochimica Acta*, v. 149, p. 21–31, <https://doi.org/10.1016/j.gca.2014.10.031>.
- Lasaga, A.C., 1995, Chapter 2. Fundamental approaches in describing mineral dissolution and precipitation rates, in *White, A.F. and Brantley, S.L., eds., Chemical Weathering Rates of Silicate Minerals: De Gruyter, Reviews in Mineralogy & Geochemistry*, v. 31 p. 23–86, <https://doi.org/10.1515/9781501509650-004>.
- Le Breton, N., and Thompson, A.B., 1988, Fluid-absent (dehydration) melting of biotite in metapelites in the early stages of crustal anatexis: *Contributions to Mineralogy and Petrology*, v. 99, p. 226–237, <https://doi.org/10.1007/BF00371463>.
- Lipman, P.W., Doe, B.R., Hedge, C.E., and Steven, T.A., 1978, Petrologic evolution of the San Juan volcanic field, southwestern Colorado: Pb and Sr isotope evidence: *Geological Society of America Bulletin*, v. 89, no. 1, p. 59–82, [https://doi.org/10.1130/0016-7606\(1978\)89<59:PEOTSJ>2.0.CO;2](https://doi.org/10.1130/0016-7606(1978)89<59:PEOTSJ>2.0.CO;2).
- López de Luchi, M.G., and Rapalini, A.E., 2002, Middle Jurassic dyke swarms in the North Patagonian Massif: the Lonco Trapial Formation in the Sierra de Mamil Choique, Rio Negro province, Argentina: *Journal of South American Earth Sciences*, v. 15, no. 6, p. 625–641, [https://doi.org/10.1016/S0895-9811\(02\)00083-4](https://doi.org/10.1016/S0895-9811(02)00083-4).
- Márquez, M., Massafarro, G., Fernández, M., Menegatti, N., and Navarrete, C., 2011, El centro volcánico Sierra Grande: caracterización petrográfica y geoquímica del magmatismo extensional liásico, Noreste de la Patagonia: *Revista de la Asociación Geológica Argentina*, v. 68, p. 555–570.
- Mattey, D., Lowry, D., and Macpherson, C., 1994, Oxygen isotope composition of mantle peridotite: *Earth and Planetary Science Letters*, v. 128, no. 3–4, p. 231–241, [https://doi.org/10.1016/0012-821X\(94\)90147-3](https://doi.org/10.1016/0012-821X(94)90147-3).
- Matthews, S.J., Atampiz, M., Omar, J.R., Valencia, V., Pérez de Arce, C., Bustos, A., Llona, F., Rodríguez, M.E., Munizaga, W., di Caro, J., Gonzalez, J., and Cingolani, C.A., 2021, Lower to Middle Jurassic volcanism and the Au-Ag mineralization at Cerro Moro District, Deseado Massif, Argentine Patagonia: *Journal of South American Earth Sciences*, v. 112, part 2, <https://doi.org/10.1016/j.jsames.2021.103622>.
- McDonough, W.F., and Sun, S.-S., 1995, The composition of the Earth: *Chemical Geology*, v. 120, no. 3–4, p. 223–253, [https://doi.org/10.1016/0009-2541\(94\)00140-4](https://doi.org/10.1016/0009-2541(94)00140-4).
- Montel, J.-M., and Vielzeuf, D., 1997, Partial melting of metagreywackes, Part II. Compositions of minerals and melts: *Contributions to Mineralogy and Petrology*, v. 128, p. 176–196, <https://doi.org/10.1007/s004100050302>.

- Moreira, P., Echeveste, H., Fernández, R., Hartmann, L.A., Santos, J.O.S., and Schalamuk, I., 2009, Dispositional age of Jurassic epithermal gold-silver ore in the Deseado Massif, Patagonia, Argentina, based on Manantial Espejo and La Josefina prospects: *Neues Jahrbuch für Geologie und Paläontologie - Abhandlungen* Band, v. 253, p. 25–40, <https://doi.org/10.1127/0077-7749/2009/0253-0025>.
- Moreira, P., Fernandez, R., Etcheverry, R., and Schalamuk, I.A., 2010, Complejos de Domos Jurásicos (~150 Ma) La Josefina y María Esther, Sector Central del Macizo del Deseado, Patagonia: *Revista de la Asociación Geológica Argentina*, v. 66, p. 335–348.
- Moreira, P., Fernández, R., Hervé, F., Fanning, C.M., and Schalamuk, I.A., 2013, Detrital zircons U-Pb SHRIMP ages and provenance of La Modesta Formation, Patagonia Argentina: *Journal of South American Earth Sciences*, v. 47, p. 32–46, <https://doi.org/10.1016/j.jsames.2013.05.010>.
- Moyen, J.-F., 2020, Granites and crustal heat budget: *Geological Society of London Special Publication* 491, 77 p., <https://doi.org/10.1144/SP491-2018-148>.
- Moyen, J.-F., Janoušek, V., Laurent, O., Bachmann, O., Jacob, J.-B., Farina, F., Fiannazza, P., and Villaros, A., 2021, Crustal melting vs. fractionation of basaltic magmas: Part 1, granites and paradigms: *Lithos*, v. 402–403, <https://doi.org/10.1016/j.lithos.2021.106291>.
- Muehlenbachs, K., 1986, Alteration of the oceanic crust and the ¹⁸O history of seawater, in Valley, J.W., Taylor, H.P., and O'Neil, J.R., *Stable Isotopes in High Temperature Geological Processes: Reviews in Mineralogy*, v. 16, p. 425–444, <https://doi.org/10.1515/9781510508936-017>.
- Navarrete, C., 2021, The volcanism of the Jurassic Chon Aike Silicic LIP influenced by Paleozoic inherited crustal structures in the northeastern Deseado Massif, Patagonia: *Journal of South American Earth Sciences*, v. 112, part 1, <https://doi.org/10.1016/j.jsames.2021.103611>.
- Navarrete, C., Gianni, G., Encinas, A., Márquez, M., Kamerbeek, Y., Valle, M., and Folguera, A., 2019, Triassic to Middle Jurassic geodynamic evolution of southwestern Gondwana: From a large flat-slab to mantle plume suction in a rollback subduction setting: *Earth-Science Reviews*, v. 194, p. 125–159, <https://doi.org/10.1016/j.earscirev.2019.05.002>.
- Navarrete, C., Butler, K.L., Hurley, M., and Márquez, M., 2020, An early Jurassic graben caldera of Chon Aike silicic LIP at the southernmost massif of the world: The Deseado caldera, Patagonia, Argentina: *Journal of South American Earth Sciences*, v. 101, <https://doi.org/10.1016/j.jsames.2020.102626>.
- Omlin, S., Räss, L., and Podladchikov, Y.Y., 2018, Simulation of three-dimensional viscoelastic deformation coupled to porous fluid flow: *Tectonophysics*, v. 746, p. 695–701, <https://doi.org/10.1016/j.tecto.2017.08.012>.
- Pamukcu, A.S., Ghiorso, M.S., and Gualda, G.A.R., 2016, High-Ti, bright-CL rims in volcanic quartz: A result of very rapid growth: *Contributions to Mineralogy and Petrology*, v. 171, article no. 105, <https://doi.org/10.1007/s00410-016-1317-x>.
- Pankhurst, R.J., and Rapela, C.R., 1995, Production of Jurassic rhyolite by anatexis of the lower crust of Patagonia: *Earth and Planetary Science Letters*, v. 134, no. 1–2, p. 23–36, [https://doi.org/10.1016/0012-821X\(95\)00103-J](https://doi.org/10.1016/0012-821X(95)00103-J).
- Pankhurst, R.J., Leat, P.T., Sruoga, P., Rapela, C.W., Márquez, M., Storey, B.C., and Riley, T.R., 1998, The Chon Aike province of Patagonia and related rocks in West Antarctica: A silicic large igneous province: *Journal of Volcanology and Geothermal Research*, v. 81, no. 1–2, p. 113–136, [https://doi.org/10.1016/S0377-0273\(97\)00070-X](https://doi.org/10.1016/S0377-0273(97)00070-X).
- Pankhurst, R.J., Riley, T.R., Fanning, C.M., and Kelley, S.P., 2000, Episodic silicic volcanism in Patagonia and the Antarctic Peninsula: Chronology of magmatism associated with the break-up of Gondwana: *Journal of Petrology*, v. 41, no. 5, p. 605–625, <https://doi.org/10.1093/petrology/41.5.605>.
- Pankhurst, R.J., Rapela, C.W., Loske, W.P., Márquez, M., and Fanning, C.M., 2003, Chronological study of the pre-Permian basement rocks of southern Patagonia: *Journal of South American Earth Sciences*, v. 16, no. 1, p. 27–44, [https://doi.org/10.1016/S0895-9811\(03\)00017-8](https://doi.org/10.1016/S0895-9811(03)00017-8).
- Parada, M.A., Palacios, C., and Lahsen, A., 1997, Jurassic extensional tectono-magmatism and associated mineralization of the El Faldeo polymetallic district, Chilean Patagonia: *Geochemical and isotopic evidence of crustal contribution: Mineralium Deposita*, v. 32, p. 547–554, <https://doi.org/10.1007/s001260050121>.
- Passchier, C.W., and Trouw, R.A.J., 1998, *Deformation Mechanisms, in Microtectonics*: Berlin, Springer, p. 25–56, https://doi.org/10.1007/978-3-662-08734-3_3.
- Patiño Douce, A.E., 1999, What do experiments tell us about the relative contributions of crust and mantle to the origin of granitic magmas?, in Castro, A., et al., eds., *Understanding Granites: Integrating New and Classical Techniques*: Geological Society of London Special Publication 168, p. 55–75, <https://doi.org/10.1144/GSL.SP.1999.168.01.05>.
- Patiño Douce, A.E., and Beard, J.S., 1995, Dehydration-melting of biotite gneiss and quartz amphibolite from 3 to 15 kbar: *Journal of Petrology*, v. 36, no. 3, p. 707–738, <https://doi.org/10.1093/petrology/36.3.707>.
- Pavón Pivetta, C., Gregori, D., Benedini, L., Garrido, M., Strazzere, L., Gerales, M., Costa dos Santos, A., and Marcos, P., 2020, Contrasting tectonic settings in Northern Chon Aike Igneous Province of Patagonia: Subduction and mantle plume-related volcanism in the Marifil formation: *International Geology Review*, v. 62, no. 15, p. 1904–1930, <https://doi.org/10.1080/00206814.2019.1669227>.
- Pearce, J.A., Harris, N.B., and Tindle, A.G., 1984, Trace element discrimination diagrams for the tectonic interpretation of granitic rocks: *Journal of Petrology*, v. 25, no. 4, p. 956–983, <https://doi.org/10.1093/petrology/25.4.956>.
- Permyu Vidal, C., Moreira, P., Guido, D.M., and Fanning, C.M., 2014, Linkages between the southern Patagonia Pre-Permian basements: New insights from detrital zircons U-Pb SHRIMP ages from the Cerro Negro District: *Geologica Acta*, v. 12, no. 2, p. 137–150, <https://doi.org/10.1344/105.000002082>.
- Poblete, J.A., Bissig, T., Mortensen, J.K., Gabites, J., Friedman, R., and Rodriguez, M., 2014, The Cerro Bayo District, Chilean Patagonia: Late Jurassic to Cretaceous magmatism and protracted history of epithermal Ag-Au mineralization: *Economic Geology*, v. 109, no. 2, p. 487–502, <https://doi.org/10.2113/econgeo.109.2.487>.
- Ramos, V.A., 2008, Patagonia: A Paleozoic continent adrift?: *Journal of South American Earth Sciences*, v. 26, no. 3, p. 235–251, <https://doi.org/10.1016/j.jsames.2008.06.002>.
- Riley, T.R., and Knight, K.B., 2001, Age of pre-break-up Gondwana magmatism: *Antarctic Science*, v. 13, no. 2, p. 99–110, <https://doi.org/10.1017/S0954102001000177>.
- Riley, T.R., Leat, P.T., Pankhurst, R.J., and Harris, C., 2001, Origins of large volume rhyolitic volcanism in the Antarctic Peninsula and Patagonia by crustal melting: *Journal of Petrology*, v. 42, no. 6, p. 1043–1065, <https://doi.org/10.1093/petrology/42.6.1043>.
- Rogers, G., and Hawkesworth, C.J., 1989, A geochemical traverse across the North Chilean Andes: Evidence for crust generation from the mantle wedge: *Earth and Planetary Science Letters*, v. 91, no. 3–4, p. 271–285, [https://doi.org/10.1016/0012-821X\(89\)90003-4](https://doi.org/10.1016/0012-821X(89)90003-4).
- Sas, M., Shane, P., Kawasaki, N., Sakamoto, N., Zellmer, G.F., and Yurimoto, H., 2022, Inter- and intra-crystal quartz $\delta^{18}\text{O}$ homogeneity at Okataina volcano, Aotearoa New Zealand: Implications for rhyolite genesis: *Journal of Volcanology and Geothermal Research*, v. 421, <https://doi.org/10.1016/j.jvolgeores.2021.107430>.
- Savin, S.M., and Epstein, S., 1970, The oxygen and hydrogen isotope geochemistry of clay minerals: *Geochimica et Cosmochimica Acta*, v. 34, no. 1, p. 25–42, [https://doi.org/10.1016/0016-7037\(70\)90149-3](https://doi.org/10.1016/0016-7037(70)90149-3).
- Seitz, S., Putlitz, B., Baumgartner, L., Escrig, S., Meibom, A., and Bouvier, A.-S., 2016, Short magmatic residence times of quartz phenocrysts in Patagonian rhyolites associated with Gondwana breakup: *Geology*, v. 44, no. 1, p. 67–70, <https://doi.org/10.1130/G37232.1>.
- Seitz, S., Baumgartner, L.P., Bouvier, A.-S., Putlitz, B., and Vennemann, T., 2017, Quartz reference materials for oxygen isotope analysis by SIMS: *Geostandards and Geoanalytical Research*, v. 41, no. 1, p. 69–75, <https://doi.org/10.1111/ggr.12133>.
- Seitz, S., Putlitz, B., Baumgartner, L.P., and Bouvier, A.-S., 2018a, The role of crustal melting in the formation of rhyolites: Constraints from SIMS oxygen isotope data (Chon Aike Province, Patagonia, Argentina): *American Mineralogist*, v. 103, no. 12, p. 2011–2027, <https://doi.org/10.2138/am-2018-6520>.
- Seitz, S., Putlitz, B., Baumgartner, L.P., Meibom, A., Escrig, S., and Bouvier, A.-S., 2018b, A nano-SIMS investigation on timescales recorded in volcanic quartz from the silicic Chon Aike Province (Patagonia): *Frontiers of Earth Science*, v. 6, <https://doi.org/10.3389/feart.2018.00095>.
- Sharp, Z.D., 2006, *Principles of Stable Isotope Geochemistry*: Prentice Hall, 360 p.
- Sharp, Z.D., Giletti, B.J., and Yoder, H.S., 1991, Oxygen diffusion rates in quartz exchanged with CO₂: *Earth and Planetary Science Letters*, v. 107, no. 2, p. 339–348, [https://doi.org/10.1016/0012-821X\(91\)90081-R](https://doi.org/10.1016/0012-821X(91)90081-R).
- Simon, L., and Lécuyer, C., 2005, Continental recycling: The oxygen isotope point of view: *Geochemistry, Geophysics, Geosystems*, v. 6, no. 8, <https://doi.org/10.1029/2005GC000958>.
- Sruoga, P., Japas, M.S., Salini, F.M., and Kleiman, L.E., 2014, La Peligrosa (47° 15'S, 71° 40'W): A key event during the Jurassic ignimbrite flare-up in Southern Patagonia, Argentina: *Journal of Volcanology and Geothermal Research*, v. 269, p. 44–56, <https://doi.org/10.1016/j.jvolgeores.2013.11.003>.
- Stevens, G., and Clemens, J.D., 1993, Fluid-absent melting and the roles of fluids in the lithosphere: A slanted summary?: *Chemical Geology*, v. 108, no. 1–4, p. 1–17, [https://doi.org/10.1016/0009-2541\(93\)90314-9](https://doi.org/10.1016/0009-2541(93)90314-9).
- Storey, B.C., and Alabaster, T., 1991, Tectonomagmatic controls on Gondwana break-up models: Evidence from the proto-Pacific margin of Antarctica: *Tectonics*, v. 10, no. 6, p. 1274–1288, <https://doi.org/10.1029/91TC01122>.

- Storey, B.C., and Kyle, P.R., 1997, An active mantle mechanism for Gondwana breakup: South African Journal of Geology, v. 100, p. 283–290.
- Storey, B., Vaughan, A., and Riley, T., 2013, The links between large igneous provinces, continental break-up and environmental change: Evidence reviewed from Antarctica: Earth and Environmental Science Transactions of the Royal Society of Edinburgh, v. 104, no. 1, p. 17–30, <https://doi.org/10.1017/S175569101300011X>.
- Strazzere, L., Pavón Pivetta, C., Gregori, D.A., Benedini, L., Geraldés, M.C., and Barros, M.V., 2022, The Marifil Volcanic Complex at Sierra de Pailemán: Implications for the Early Jurassic magmatic evolution of the Eastern North Patagonian Region: International Geology Review, v. 64, no. 6, <https://doi.org/10.1080/00206814.2021.1884996>.
- Suárez, R., González, P.D., and Ghiglione, M.C., 2019, A review on the tectonic evolution of the Paleozoic–Triassic basins from Patagonia: Record of protracted westward migration of the pre-Jurassic subduction zone: Journal of South American Earth Sciences, v. 95, <https://doi.org/10.1016/j.jsames.2019.102256>.
- Taylor, H.P., 1974, The application of oxygen and hydrogen isotope studies to problems of hydrothermal alteration and ore deposition: Economic Geology, v. 69, no. 6, p. 843–883, <https://doi.org/10.2113/gsecongeo.69.6.843>.
- Taylor, H.P., 1980, The effects of assimilation of country rocks by magmas on $^{18}\text{O}/^{16}\text{O}$ and $^{87}\text{Sr}/^{86}\text{Sr}$ systematics in igneous rocks: Earth and Planetary Science Letters, v. 47, no. 2, p. 243–254, [https://doi.org/10.1016/0012-821X\(80\)90040-0](https://doi.org/10.1016/0012-821X(80)90040-0).
- Taylor, H.P., and Sheppard, S.M.F., 1986, Igneous rocks; I, Processes of isotopic fractionation and isotope systematics, in Valley, J.W., Taylor, H.P., and O'Neil, J.R., Stable Isotopes in High Temperature Geological Processes: Reviews in Mineralogy and Geochemistry, v. 16, p. 227–272, <https://doi.org/10.1515/9781501508936-013>.
- Thompson, A.B., 1982, Dehydration melting of crustal rocks and the generation of H_2O -undersaturated granitic liquids: American Journal of Science, v. 282, no. 10, p. 1567–1595, <https://doi.org/10.2475/ajs.282.10.1567>.
- Thompson, A.B., and Connolly, J.A.D., 1995, Melting of the continental crust: Some thermal and petrological constraints on anatexis in continental collision zones and other tectonic settings: Journal of Geophysical Research, v. 100, no. B8, p. 15,565–15,579, <https://doi.org/10.1029/95JB00191>.
- Valley, J.W., 2003, Oxygen Isotopes in Zircon: Reviews in Mineralogy and Geochemistry, v. 53, no. 1, p. 343–385, <https://doi.org/10.2113/0530343>.
- Valley, J.W., Lackey, J.S., Cavosie, A.J., Clenchnko, C.C., Spicuzza, M.J., Basei, M.A.S., Bindeman, I.N., Ferreira, V.P., Sial, A.N., King, E.M., Peck, W.H., Sinha, A.K., and Wei, C.S., 2005, 4.4 billion years of crustal maturation: Oxygen isotope ratios of magmatic zircon: Contributions to Mineralogy and Petrology, v. 150, p. 561–580, <https://doi.org/10.1007/s00410-005-0025-8>.
- Vielzeuf, D., and Montel, J.-M., 1994, Partial melting of metagreywackes. Part I. Fluid-absent experiments and phase relationships: Contributions to Mineralogy and Petrology, v. 117, p. 375–393, <https://doi.org/10.1007/BF00307272>.
- Wark, D.A., and Watson, E.B., 2006, TitanioQ: A titanium-in-quartz geothermometer: Contributions to Mineralogy and Petrology, v. 152, p. 743–754, <https://doi.org/10.1007/s00410-006-0132-1>.
- Watts, K.E., John, D.A., Colgan, J.P., Henry, C.D., Bindeman, I.N., and Schmitt, A.K., 2016, Probing the volcanic-plutonic connection and the genesis of crystal-rich rhyolite in a deeply dissected supervolcano in the Nevada Great Basin: Source of the Late Eocene Caetano Tuff: Journal of Petrology, v. 57, no. 8, p. 1599–1644, <https://doi.org/10.1093/ptrology/egw051>.
- Watts, K.E., John, D.A., Colgan, J.P., Henry, C.D., Bindeman, I.N., and Valley, J.W., 2019, Oxygen isotopic investigation of silicic magmatism in the Stillwater caldera complex, Nevada: Generation of large-volume, low- $\delta^{18}\text{O}$ rhyolitic tuffs and assessment of their regional context in the Great Basin of the western United States: Geological Society of America Bulletin, v. 131, no. 7–8, p. 1133–1156, <https://doi.org/10.1130/B35021.1>.
- Wever, H.E., and Storey, B.C., 1992, Bimodal magmatism in northeast Palmer Land, Antarctic Peninsula: Geochemical evidence for a Jurassic ensialic back-arc basin: Tectonophysics, v. 205, no. 1–3, p. 239–259, [https://doi.org/10.1016/0040-1951\(92\)90429-A](https://doi.org/10.1016/0040-1951(92)90429-A).
- Winchester, J.A., and Floyd, P.A., 1977, Geochemical discrimination of different magma series and their differentiation products using immobile elements: Chemical Geology, v. 20, p. 325–343, [https://doi.org/10.1016/0009-2541\(77\)90057-2](https://doi.org/10.1016/0009-2541(77)90057-2).
- Yardley, B.D., and Valley, J.W., 1997, The petrologic case for a dry lower crust: Journal of Geophysical Research, v. 102, no. B6, p. 12,173–12,185, <https://doi.org/10.1029/97JB00508>.
- Zaffarana, C.B., Lagorio, S.L., Gallastegui, G., Wörner, G., Orts, D.L., Gregori, D., Poma, S., Busteros, A., Giacosa, R., Nieto, D.S., González, V.R., Boltshauser, B., Negre, C.P., and Haller, M., 2020, Petrogenetic study of the Lonco Trapial volcanism and its comparison with the Early-Middle Jurassic magmatic units from northern Patagonia: Journal of South American Earth Sciences, v. 101, <https://doi.org/10.1016/j.jsames.2020.102624>.
- Zhao, Z.-F., and Zheng, Y.F., 2003, Calculation of oxygen isotope fractionation in magmatic rocks: Chemical Geology, v. 193, no. 1–2, p. 59–80, [https://doi.org/10.1016/S0009-2541\(02\)00226-7](https://doi.org/10.1016/S0009-2541(02)00226-7).